# STARBENCH: the D-type expansion of an H II region

Bisbas, T.G.; Haworth, T.J.; Williams, R.J.R.; Mackey, J.; Tremblin, P.; Raga, A.C.; ... ; Wünsch, R.

# STARBENCH: the D-type expansion of an H II region

T. G. Bisbas,[1,2,3]★ T. J. Haworth,[4]★ R. J. R. Williams,[5] J. Mackey,[6,7]★ P. Tremblin,[8,9]
A. C. Raga,[10] S. J. Arthur,[11] C. Baczynski,[12] J. E. Dale,[13,14] T. Frostholm,[15] S. Geen,[16]
T. Haugbølle,[15] D. Hubber,[13,14] I. T. Iliev,[17] R. Kuiper,[18,19] J. Rosdahl,[20] D. Sullivan,[17]
S. Walch[7] and R. Wünsch[21]

*Affiliations are listed at the end of the paper*

## ABSTRACT

STARBENCH is a project focused on benchmarking and validating different star formation and stellar feedback codes. In this first STARBENCH paper we perform a comparison study of the D-type expansion of an H II region. The aim of this work is to understand the differences observed between the 12 participating numerical codes against the various analytical expressions examining the D-type phase of H II region expansion. To do this, we propose two well-defined tests which are tackled by 1D and 3D grid- and smoothed particle hydrodynamics-based codes. The first test examines the 'early phase' D-type scenario during which the mechanical pressure driving the expansion is significantly larger than the thermal pressure of the neutral medium. The second test examines the 'late phase' D-type scenario during which the system relaxes to pressure equilibrium with the external medium. Although they are mutually in excellent agreement, all 12 participating codes follow a modified expansion law that deviates significantly from the classical Spitzer solution in both scenarios. We present a semi-empirical formula combining the two different solutions appropriate to both early and late phases that agrees with high-resolution simulations to $\lesssim 2$ per cent. This formula provides a much better benchmark solution for code validation than the Spitzer solution. The present comparison has validated the participating codes and through this project we provide a data set for calibrating the treatment of ionizing radiation hydrodynamics codes.

**Key words:** hydrodynamics – methods: numerical – ISM: bubbles – H II regions – ISM: kinematics and dynamics – galaxies: ISM.

## 1 INTRODUCTION

Computer simulations play an increasingly important role in astrophysics. They allow researchers to apply theoretical understanding to complex systems beyond the capability of analytic calculation, and also provide validation for the physical correctness of proposed theoretical models. However, computational models have their own sources of error. It is therefore important to validate their accuracy, where possible, if their results are to have any credence. Different sources of error require different validation techniques, but use of code intercomparisons and resolution studies for well-defined test problems is particularly powerful in this regard. Previous such comparisons have included photoionization modelling (Péquignot et al. 2001), PDR code comparison (Röllig et al. 2007), and cosmological code comparison (Iliev et al. 2006, 2009).

As well as the standard tests which are widely applied to computational hydrodynamics codes, such as Sod shock tubes (Sod 1978) and the Sedov–Taylor point explosion (Sedov 1959; Taylor 1950), it is important to develop test problems more specific to the domain of study, which test broader physics couplings. The STARBENCH project seeks to develop a collection of well-understood validation cases for the modelling of star-forming regions. To date, two workshops have been held (Exeter, 2013 April; Bonn, 2014 September),[1] in which groups specializing in numerical star formation have gathered to set the basis of standard and well-defined tests and explore the differences observed between their codes. The present paper reports the results of the first test investigated by the STARBENCH project: the D-type expansion of an H II region.

The problem of the expansion of an H II region into a uniform neutral medium has a long history in theoretical and numerical

---

★ E-mail: tb@mpe.mpg.de (TGB); thaworth@ast.cam.ac.uk (StarBench-I, TJH); mackey@ph1.uni-koeln.de (StarBench-II, JM)

[1] STARBENCH-I: http://www.astro.ex.ac.uk/people/haworth/workshop_bench/index.html STARBENCH-II: https://www.astro.uni-bonn.de/sb-ii/index.html

studies of the interstellar medium (ISM). The ionizing photons ($h\nu > 13.6$ eV) produced by a hot, massive star ionize and heat a volume of gas around the star, which then begins to expand supersonically into the surrounding medium due to the overpressure. The photoionized region is bounded by an ionization front, which separates the ionized from the neutral gas. Kahn ([1954](#)) and Axford ([1961](#)) showed analytically that the ionization front relatively quickly switches from R-type to D-type and drives a strong shock into the neutral ISM. This behaviour was verified by early numerical investigations of H II region expansion conducted by Mathews ([1965](#)) and Lasker ([1966](#)). These early analytic and numerical calculations are reviewed by Mathews & O'Dell ([1969](#)), and subsequent developments, including the first multidimensional simulations in uniform and non-uniform media, are reviewed by Yorke ([1986](#)). An analytic solution for the expansion rate of the H II region during the D-type phase as a function of time was derived by Spitzer ([1978](#)), which is presented more lucidly in the book of Dyson & Williams ([1980](#)). This has become the standard solution with which numerical results are compared.

Most modern code developers use the spherical expansion of an H II region as a standard test problem to validate their coupled photoionization and (magneto-)hydrodynamics algorithms (e.g. Mellema et al. [2006b](#); Krumholz, Stone & Gardiner [2007](#); Mackey & Lim [2010](#), [2011](#); Raga et al. [2012b](#); Tremblin et al. [2012a](#)). This problem involves a complicated combination of fluid dynamics, radiative transfer, microphysical heating, cooling, ionization and recombination, and differences between results obtained with different codes and algorithms have not so far been addressed in any depth in the literature. There is therefore a pressing need of setting up benchmarking tests to examine the behaviour of the different codes in reproducing known analytical expressions.

Although the Spitzer ([1978](#)) analytical solution is widely used for code testing, alternative analytical solutions for the expansion of an H II region, applicable at different stages of the evolution and based on different assumptions, have been developed more recently, such as those of Hosokawa & Inutsuka ([2006](#)) and Raga et al. ([2012a,b](#)). It is an aim of the present paper to determine which, if any, of the available analytical solutions is most suitable, and thus to provide a benchmark useful for any other radiation hydrodynamics code. For instance, in the first attempts of the present test, several discrepancies between the codes have been identified resulting from bugs or incorrect assumptions which have all been fixed throughout this work. This demonstrates the value of such a comparison in improving confidence in the accuracy of these codes when applied to more complex scenarios.

The interest of the authors of the present paper in establishing a reliable benchmark test for expanding H II regions stems from the large body of work, much of it done in the last decade, on the influence of expanding H II regions at and below giant molecular cloud (GMC) scales, intended to explore explicitly the role of photoionization in the evolution and destruction/dispersal of GMCs and the regulation of star formation rates and efficiencies. H II region feedback has been invoked both as a trigger of star formation (e.g. Elmegreen & Lada [1977](#)), and as the main agent responsible for terminating it (e.g. McKee, van Buren & Lazareff [1984](#); Matzner [2002](#)). Many simulations have sought to model one or both of these scenarios in order to establish whether the influence of photoionizing feedback on the galactic star formation process is overall positive or negative.

For example, the gravitational instability of the dense shells driven by H II regions, often referred to as the 'collect and collapse' process has been modelled by Elmegreen & Lada ([1977](#)), Whitworth et al. ([1994a,b](#)), and Dale, Bonnell & Whitworth ([2007](#)), who show

that, in principle, it should be an efficient means of triggering star formation in even smooth media. Other authors have instead studied the influence of substructure encountered by the radiation field, either in terms of well-defined isolated clumps and the radiation-driven implosion model (Bertoldi [1989](#); Lefloch & Lazareff [1994](#); Mellema et al. [1998](#); Kessel-Deynet & Burkert [2003](#); Mackey & Lim [2011](#); Bisbas et al. [2011](#); Mackey & Lim [2011](#); Haworth & Harries [2012](#)), or of more generalized fractal substructure (Colella & Woodward [1984](#); LeVeque [2002](#); Walch et al. [2012](#), [2013](#), [2015](#)).

The negative effects of H II region expansion on clouds already in a dynamical state have also received much attention. Peters et al. ([2010](#)) and Peters et al. ([2011](#)) model H II regions driven by roughly centrally-located massive stars on rotating GMCs, finding them rather ineffective at preventing the formation of stars. The general problem of the interaction of expanding H II regions with turbulent media has been modelled by Mellema et al. ([2006b](#)), Gritschneder et al. ([2009](#)), Arthur et al. ([2011](#)), Tremblin et al. ([2012b](#)), Dale, Ercolano & Bonnell ([2012](#)), Colín, Vázquez-Semadeni & Gómez ([2013](#)), and Boneberg et al. ([2015](#)), most of whom conclude that H II regions are able to drive turbulence, and are destructive to GMCs of $\sim 10^4\,M_\odot$.

This paper is organized as follows. In Section 2, we present a theoretical background of the D-type expansion of an H II region and discuss the different analytical solutions to this problem. In Section 3 we present the numerical codes participating in this test, highlighting in brief the methods used to propagate the ionizing radiation. In Section 4, we present the initial conditions of the benchmarking test and in Section 5 we show the results. We summarize and conclude in Section 6.

## 2 THEORETICAL BACKGROUND

A hot, massive star emits large numbers of extreme ultraviolet (EUV) photon with energy $h\nu$ larger than the ionization potential of hydrogen (13.6eV). The ionizing photons interact with the surrounding neutral medium and ionize a volume of gas within which the rate of ionizations is nearly balanced by recombinations with the remaining small flux ionizing the neutral material passing through its surface. The kinetic energy of the ejected photoelectrons heats the gas within the photoionized volume by collisions but efficient cooling due to collisionally excited line radiation of metal ions such as doubly ionized oxygen means that temperatures inside H II regions are approximately uniform and typically $\sim 10^4$ K (see Osterbrock [1989](#), for details). In the analysis that follows, we will ignore the detailed physical processes and make a series of simplifying assumptions.

Consider a spherically symmetric cloud of radius $R_{cl}$, of total mass $M_{cl}$ and of uniform density $\rho_{cl}$ consisting of pure atomic hydrogen with a uniform temperature $T_{cl}$. Let us place a radiation source at the centre of the cloud which defines the origin of a Cartesian coordinate system. The source emits $\dot{\mathcal{N}}_{LyC}$ Lyman continuum ionizing photons per unit time and we assume that the ionizing photons are monochromatic with energy $h\nu = 13.6$ eV. We assume a photoionization cross-section of $\bar{\sigma} = 6.3 \times 10^{-18}$ cm$^2$ and we use the recombination coefficient, $\alpha_B$, into excited stages only by invoking the *on-the-spot* approximation (Osterbrock [1989](#), known as the 'case-B' recombination coefficient). Assuming an isothermal H II region at $T_i = 10^4$ K the case-B recombination coefficient is taken to be $\alpha_B \simeq 2.7 \times 10^{-13}$ cm$^3$ s$^{-1}$. Hereafter, the indices 'i' and 'o' shall denote the ionized and the neutral medium, respectively.

Strömgren ([1939](#)) was the first to show that the transition zone between the ionized gas and the surrounding neutral medium occurs

over a very short distance compared to the dimensions of the H II region. This transition zone is the *ionization front* and we can treat it as a sharp discontinuity. The distance over which the degree of ionization changes from 90 per cent to 10 per cent is given by

$$\Delta R_{St} \simeq \frac{20 m_p}{\rho_o \bar{\sigma}} \simeq 1.72 \times 10^{-4} \, \text{pc} \left( \frac{\rho_o}{10^{-20} \, \text{g cm}^{-3}} \right)^{-1}, \qquad (1)$$

(e.g. Whitworth, private communication) where $m_p$ represents the proton mass.

Kahn (1954) studied in detail the propagation of an ionization front into a neutral medium when an ionizing star suddenly switches on. At early times most of the Lyman continuum photons ionize additional gas beyond the instantaneous position of the ionization front. Thus the H II region expands rapidly at highly supersonic speed relative to the sound speed of the ionized gas. In this first phase the ionization front is called *R-type* (R=Rarefied). As shown by Strömgren (1939), the $\dot{\mathcal{N}}_{LyC}$ photons emitted by the central source will ionize a spherical region of radius

$$R_{St} = \left( \frac{3 \dot{\mathcal{N}}_{LyC} m_p^2}{4 \pi \alpha_B \rho_o^2} \right)^{1/3}, \qquad (2)$$

where $\rho_o = \rho_{cl}$ and $m_p$ is the proton mass. Hereafter, we refer to the spherical region of radius $R_{St}$ as the *initial Strömgren sphere* and the radius $R_{St}$ as the *initial Strömgren radius*. The R-type phase of expansion terminates once the ionization front reaches this initial Strömgren radius. The time-scale for this first phase is of order the recombination time

$$t_D = \frac{m_p}{\alpha_B \rho_o} \simeq 19.6 \, \text{yr} \left( \frac{\rho_o}{10^{-20} \, \text{g cm}^{-3}} \right)^{-1}. \qquad (3)$$

The large temperature difference between the two regions results in a large difference in thermal pressure, and the H II region expands. In this second phase, which is called *D-type* (D=Dense), the ionization front propagates at subsonic speed relative to the ionized gas but at supersonic speed relative to the neutral gas. Therefore, it is preceded by a *shock front* which sweeps up a dense shell of neutral gas. The shell is bounded on its inside by the ionization front and on its outside by the shock front.

Within the ionized region we assume that at all times there is a balance between the ionizing photons produced by the star and the recombination events. Therefore,

$$\dot{\mathcal{N}}_{LyC} = \int \frac{\rho_i \rho_e}{m_p m_e} \alpha_B dV, \qquad (4)$$

where $\rho_e$ and $m_e$ are the electron density and mass, respectively. If we assume that (i) the medium is entirely ionized, (ii) $\rho_e = \rho_i m_e / m_p$, and (iii) that the ionization front has a sharp edge, the above integral leads to

$$\dot{\mathcal{N}}_{LyC} = \frac{4\pi}{3} \left\{ \frac{\rho_i(t)}{m_p} \right\}^2 \alpha_B R_{IF}^3(t), \qquad (5)$$

which, when combined with equation (2), gives

$$\rho_i(t) = \rho_o \left\{ \frac{R_{St}}{R_{IF}(t)} \right\}^{3/2}, \qquad (6)$$

where $R_{IF}$ is the extend of the ionized region. As the H II region expands, it ionizes more neutral gas and its mass increases in time. The time-dependent mass of the ionized region, $M_i(t)$ is given by

$$M_i(t) = \frac{4\pi}{3} \rho_o R_{St}^{3/2} R_{IF}^{3/2}(t). \qquad (7)$$

The thermal pressure of the ionized gas in an H II region (which drives the expansion) matches approximately with the thermal pressure of the neutral gas in the shell between the ionization front and the shock front.

### 2.1 Early-time behaviour

#### 2.1.1 Spitzer approximation

The first analytical attempt to model the D-type expansion of an H II region was performed by Spitzer (1978) which was investigated in more depth by Dyson & Williams (1980). As pointed out by Raga et al. (2012b), by assuming the thin shell approximation and by equating the pressure of the neutral gas in the shell between the ionization front and the shock front with the ram pressure of the undisturbed neutral gas as it is swept up by the shock front we obtain

$$\frac{1}{c_i} \frac{dR_{Sp}(t)}{dt} = \left\{ \frac{R_{St}}{R_{Sp}(t)} \right\}^{3/4} - \frac{\mu_i T_o}{\mu_o T_i} \left\{ \frac{R_{St}}{R_{Sp}(t)} \right\}^{-3/4}, \qquad (8)$$

where $\mu$ is the mean molecular weight of the gas. The above equation shall be referred to as 'Raga-I' throughout this paper.

The ratio $\mu_i T_o / \mu_o T_i$ found on the right-hand side of equation (8) is generally small ($\sim 1/200$). At early times the term $\frac{\mu_i T_o}{\mu_o T_i} \left\{ \frac{R_{St}}{R_{Sp}(t)} \right\}^{-3/4}$ can be neglected, therefore equation (8) leads to the so-called Spitzer solution:

$$R_{Sp}(t) = R_{St} \left( 1 + \frac{7}{4} \frac{c_i t}{R_{St}} \right)^{4/7}. \qquad (9)$$

#### 2.1.2 Hosokawa–Inutsuka approximation

A different approach describing the expansion of an H II region was provided by Hosokawa & Inutsuka (2006), who derived the position of the ionization front in time directly from the equation of motion of the expanding shell. Independently, Raga et al. (2012a) argued that the differential equation (8) does not incorporate the inertia of the shocked neutral gas which is created during the expansion of the H II region. To include the inertia, we may write the equation CAPREOLE-C²-RAY of motion of the mass $M$ within the shocked shell as

$$\frac{d}{dt}(M \dot{R}_{HI}) = 4\pi R_{HI}^2 (P_i - P_o), \qquad (10)$$

where $P$ is the thermal pressure of the gas and $R_{HI}$ is the position of the shell as modelled by Hosokawa & Inutsuka (2006, 'HI'). The term $P_i - P_o$ corresponds to the net thermal pressure taking into account the pressure acting from the neutral gas on to the ionized gas. Using equation (6) and where $R_{IF}(t)$ represents now the position of the shocked shell $R_{HI}$, we obtain the second-order non-linear differential equation

$$\ddot{R}_{HI} + \left( \frac{3}{R_{HI}} \right) \dot{R}_{HI}^2 = \frac{3 R_{St}^{3/2} c_i^2}{R_{HI}^{5/2}} - \frac{3 c_o^2}{R_{HI}}. \qquad (11)$$

The above equation shall be referred to as 'Raga-II' throughout this paper. Equation (11) represents the equation of motion of the expanding shell when its inertia is taken into account. Solving the above leads to

$$\dot{R}_{HI}(t) = c_i \sqrt{\frac{4}{3} \frac{R_{St}^{3/2}}{R_{HI}^{3/2}(t)} - \frac{\mu_i T_o}{2 \mu_o T_i}}. \qquad (12)$$

At early times we may neglect the $\mu_i T_o / \mu_o T_i$ term. This corresponds to the assumption of $P_o = 0$ in equation (10). Equation (12) has

**Table 1.** Participating codes in this project.

| Code name | Code representative(s) | Kind | Early phase 1D | Early phase 3D | Late phase 1D | Late phase 3D | Mesh motion | Mesh geometry[a] |
|---|---|---|---|---|---|---|---|---|
| AQUILINE | Williams | Grid | X | | X | | Eulerian | Uniform AMR radial |
| CAPREOLE-C$^2$-RAY | Arthur | Grid | | X | | X | Eulerian | Uniform Cartesian |
| FLASH-FERVENT | Baczynski | Grid | | X | | X | Eulerian | Uniform Cartesian |
| FLASH-TREERAY | Wünsch | Grid | | X | | X | Eulerian | Uniform Cartesian |
| GLIDE | Williams | Grid | X | | X | | Lagrangian | Uniform radial |
| HERACLES | Tremblin | Grid | X | | X | | Eulerian | Uniform radial |
| PION | Mackey | Grid | X | X | X | X | Eulerian | Uniform radial (1D) Cartesian (3D) |
| RAMSES-LAMPRAY | Haugbølle & Frostholm | Grid | | X | | | Eulerian | Uniform Cartesian |
| RAMSES-RT | Geen & Rosdahl | Grid | | X | | X | Eulerian | Uniform Cartesian |
| SEDNA | Kuiper | Grid | X | X | X | X | Eulerian | Uniform radial |
| SEREN | Hubber & Bisbas | SPH | | X | | X | Lagrangian (SPH) | Equal mass |
| TORUS | Haworth | Grid | X | | X | | Eulerian | Uniform radial |

*Notes.* [a]Refers to the test problem presented in this paper and not to the general capabilities of each code.

therefore the analytical solution

$$R_{HI}(t) = R_{St} \left(1 + \frac{7}{4}\sqrt{\frac{4}{3}}\frac{c_i t}{R_{St}}\right)^{4/7}. \tag{13}$$

This equation was first presented by Hosokawa & Inutsuka (2006) and it differs from the known Spitzer expression (equation 9) by a $\sqrt{4/3}$ factor. This factor arises from our inclusion of the inertia of the shocked gas due to its own movement leading to a slightly faster expansion than that obtained from equation (9).

## 2.2 Late-time behaviour

### 2.2.1 Raga's extension of Spitzer (Raga-I)

At later times the term $\frac{\mu_i T_o}{\mu_o T_i}\left\{\frac{R_{St}}{R_{Sp}(t)}\right\}^{-3/4}$ increases and eventually the H II region stagnates at $t = t_{STAG}$ which is defined by $\dot{R}_{Sp}(t_{STAG}) = 0$. By this time the H II region is in pressure equilibrium, thus it does not expand further. The stagnation radius is (from equation 8)

$$R_{STAG} = \left(\frac{c_i}{c_o}\right)^{4/3} R_{St}, \tag{14}$$

the density of the ionized gas is (from equation 6)

$$\rho_i = \rho_o \left(\frac{c_o}{c_i}\right)^2, \tag{15}$$

and the total ionized mass is (from equation 7)

$$M_i(t_{STAG}) = \frac{4\pi}{3} R_{St}^3 \rho_o \left(\frac{c_i}{c_o}\right)^2. \tag{16}$$

### 2.2.2 Raga's extension of Hosokawa–Inutsuka (Raga-II)

At later times $R_{HI}$ becomes large, and therefore the two terms contained in the square root of equation (12) become comparable. Eventually at $t = t_{STAG}$ in which $\dot{R}_{HI}(t_{STAG}) = 0$ we obtain the stagnation radius

$$R_{STAG} = R_{St}\left(\frac{8}{3}\right)^{2/3}\left(\frac{c_i}{c_o}\right)^{4/3}, \tag{17}$$

the density of the ionized medium

$$\rho_i = \rho_o \left(\frac{8}{3}\right)^{2/3}\left(\frac{c_o}{c_i}\right)^{4/3}, \tag{18}$$

and the total ionized mass

$$M_i(t_{STAG}) = \frac{4\pi}{3} R_{St}^3 \rho_o \left(\frac{8}{3}\right)^{8/3}\left(\frac{c_i}{c_o}\right)^{8/3}. \tag{19}$$

## 3 NUMERICAL CODES

The methods[2] which the present numerical codes used to account for hydrodynamics are either grid-based techniques (e.g. Colella & Woodward 1984; Roe 1986; Berger & Colella 1989) or smoothed particle hydrodynamics based techniques (SPH; e.g. Gingold & Monaghan 1977; Lucy 1977). Here, we present a brief review of the participating codes and their radiative transfer capabilities. All codes are summarized in Table 1.

### 3.1 AQUILINE, GLIDE (RJRW)

AQUILINE is a simplified version of AQUALUNG (Williams 2000), restricted to one-dimensional problems. It has been extended to treat problems in spherical coordinates. Mesh refinement is implemented by bisection of cells, with simple gradient-based refinement criteria. It is based on a second-order MUSCL scheme using an exact Riemann solver, as in Falle (1991); some improvements have been made to the robustness and accuracy of the Riemann solution in extreme limits. It uses a photon-conservative scheme for the interaction of the ionizing radiation with the gas, as discussed in Williams (2002), but including the obvious modifications for spherical geometry.

GLIDE is a one-dimensional Lagrangian code, based on the same underlying Riemann solver and ionization/radiation solve as AQUALUNG (Williams 2002). This code uses piecewise-linear reconstruction within mesh cells; however, the interface velocities and pressures calculated by the Riemann solver are used to advance the zone widths, momenta and energies directly, rather than being converted into fluxes. In the calculations presented, the zones have been taken to have constant initial spatial width.

For both of these codes, the hydrodynamical advance was made using $\gamma = 5/3$; testing has shown that this makes a minimal difference from $\gamma$ close to unity, due the close coupling of the radiation step (at both half- and full-step).

---

[2] It is not the scope of this paper to describe each hydrodynamical method. We redirect the reader to the cited works for further details.

## 3.2 CAPREOLE-C$^2$-RAY (G. Mellema and SJA)

The CAPREOLE-C$^2$-RAY radiation-hydrodynamics code combines the non-relativistic Roe solver PPM scheme described in Eulderink & Mellema (1995) with the radiation transport and photoionization code C$^2$-RAY (Conservative Causal ray) code developed by Mellema et al. (2006a). This code has been used to model the expansion of H II regions in turbulent molecular clouds (Mellema et al. 2006b; Medina et al. 2014) and for these applications the various contributions to the heating and cooling in the photoionized and neutral gas are treated by analytical fits, as described in Henney et al. (2009). For the present benchmark test, a simple non-equilibrium prescription for thermal balance has been included, which ensures a temperature of $10^4$ K in the ionized gas and $10^2$ K or $10^3$ K, as required, in the neutral gas. The calculations are all performed on a fixed, uniform Cartesian grid in three dimensions and limited parallelization using Open-MP has been implemented.

## 3.3 FLASH-FERVENT (CB)

FERVENT (Baczynski, Glover & Klessen 2015) is a multisource, Cartesian, radiative transfer code module implemented in the magnetohydrodynamical grid code FLASH 4 (Fryxell et al. 2000; Dubey, Reid & Fisher 2008). It is based on an adaptively split ray-tracing scheme introduced in Wise & Abel (2011). Rays are initially cast from a spherically uniform distribution based on the HEALPIX decomposition (Górski et al. 2005). They intersect and traverse the domain until a splitting criterion is fulfilled, based on the apparent pixel size in comparison to the cell face area. In this way a full sampling of the mesh domain is guaranteed. Each cell of the mesh is intersected by multiple non-aligned rays, which ensures that artefacts from the underlying Cartesian mesh are eliminated. Additionally, the HEALPIX sphere is rotated in each time-step to wash out any remaining alignment effects.

It is fully Message Passing Interface (MPI)-parallelized by employing asynchronous communication, i.e. as soon as a ray leaves the local domain it is sent to its neighbour. This has the advantage that domains without any point sources of their own are involved as soon as possible instead of having to wait until the neighbour completely sampled its domain.

Ionizing radiation is modelled in a photon conservative, mesh resolution independent fashion. Photon conservation is guaranteed by an incremental attenuation of the photon flux $dN = N(1 - e^{-d\tau})$, where the flux $N$ that enters a neighbouring cell $i+1$ is $N_{i+1} = N_i - dN_i$. $N$ is given as an absolute photon number $N = P\Delta t$, with $P$ in s$^{-1}$. An ionization rate is calculated by exploiting the fact that $dN$ is a dimensionless quantity which implicitly takes the dimensionality $m$ of the size of the cell $V_{cell} = d^m$ into account. The ionization rate is then given as $k_{ion} = dN_{ion}/(n_H V_{cell} \Delta t)$. The speed of the I-front expansion is captured by enforcing that the change in the abundance of atomic hydrogen, $|\Delta x_{H,new} - \Delta x_{H,old}| = \Delta x_H$ is smaller than 10 per cent.

Additionally, FERVENT is fully coupled to a reduced chemical network (Glover & Mac Low 2007a,b; Glover et al. 2010; Glover & Clark 2012; Walch et al. 2014). It explicitly tracks the species CO, C$^+$, H$^+$, H and H$_2$ which allows for a realistic chemical composition and hence a direct way to compare to observations. Moreover, it accounts for most heating processes by non-ionizing radiation, such as UV photodissociation, vibrational pumping and photoelectric heating.

## 3.4 FLASH-TREERAY (RW)

TREERAY (Wünsch et al., in preparation) is a new radiation transport method combining a tree code with reverse ray tracing. It has been implemented into the hydrodynamic code FLASH (Fryxell et al. 2000, version 4.2.1 used in this work). The TREERAY method has several advantages that make it suitable for being coupled with hydrodynamic codes. Particularly, (i) it is relatively fast (costs are similar to solving for self-gravity), (ii) the calculation time does not depend on number of sources (making it ideal for diffuse radiation treatment), (iii) ray tracing has the highest resolution close to the point where the intensity is calculated, and (iv) it is relatively easy to parallelize this algorithm on distributed memory architectures. The disadvantage is that distant sources and regions of absorption are smoothed over a larger volume leading to the artificial numerical diffusion of radiation.

The algorithm kernel consists of three steps. In the first one, sources of radiation and the absorbing gas are mapped on to the octal tree and the emission and absorption coefficients are calculated for each tree node. In the second step, the tree is traversed for each grid cell and tree nodes are mapped on to rays going in all directions. The ray directions are obtained using the HEALPIX library for uniform tessellation of the surface of a sphere (Górski et al. 2005), and the mapping coefficients are proportional to the volume of the intersection of each tree node with the cone associated with the ray. In this way, no absorbing or emitting gas is omitted. In the third step, the one-dimensional radiation transport equation is solved along each ray. This computational kernel is called in each hydrodynamic time-step iteratively, until the radiation field converges, in order to account for regions irradiated from several different directions.

Various physical processes can be implemented into the code by providing prescriptions for the absorption and the emission coefficients. In this work, we use a simple on-the-spot approximation with only one source emitting a constant number of EUV photons per unit time and the number of absorbed photons given by the recombination rate to higher-than-ground levels.

## 3.5 HERACLES (PT)

HERACLES[3] (González, Audit & Huynh 2007; Audit et al. 2011) is a 3D[4] hydrodynamical code used to simulate astrophysical fluid flows. It uses a finite volume method on fixed grids to solve the equations of hydrodynamics, magnetohydrodynamic (MHD), radiative transfer and gravity. This software is developed at the Service d'Astrophysique, CEA/Saclay as part of the COAST project and is registered under the CeCILL license.

HERACLES simulates astrophysical fluid flows using a grid based Eulerian finite volume Godunov method. It is capable of simulating pure hydrodynamical flows, MHD flows, radiation hydrodynamic flows (using either flux limited diffusion or the M1 moment method), self-gravitating flows using a Poisson solver or all of the above. HERACLES uses Cartesian, spherical and cylindrical grids. Current ongoing developments include a multigrid method and a multigroup scheme for the radiative transfer.

The ionization scheme is described in Tremblin et al. (2011) and was applied to the study of the formation of pillars and globules at the interface of H II regions and turbulent molecular clouds (see Tremblin et al. 2012a,b).

---

[3] http://irfu.cea.fr/Projets/Site_heracles
[4] Here used as 1D only.

### 3.6 PION (JM)

PION is an Eulerian MHD code that solves either the Euler equations of gas dynamics (Mackey & Lim 2010) or the ideal MHD equations (Mackey & Lim 2011) on a uniform fixed mesh in Cartesian (1D, 2D, 3D), cylindrical (2D axisymmetric), or spherical (1D) coordinates. It uses a finite volume, shock-capturing integration scheme (Falle, Komissarov & Joarder 1998) with geometric source terms to account for curvilinear coordinates when needed (Falle 1991). Abundances of chemical species and tracers are passively advected with the flow. PION is written in C++, is designed to be as modular as possible, is parallelized with MPI by dividing the domain into *N* subdomains (*N* must be a power of 2), each controlled by one MPI process, and scales well to at least 1024 cores for 3D simulations.

Radiative transfer of ionizing and non-ionizing photons from point sources and sources at infinity is followed using a short characteristics raytracer to calculate column densities. This is coupled to a microphysics module to solve the rate equations for chemical species and their associated heating or cooling. Scattered and re-emitted photons are treated using the 'on-the-spot' approximation, i.e. they are assumed to be re-absorbed locally. A photon-conserving formulation of the ionization rates is used and spectral hardening of ionizing radiation with optical depth is included (following Mellema et al. 2006a). The non-equilibrium ionization of H is integrated together with the thermal evolution of the gas using CVODE (Cohen, Hindmarsh & Dubois 1996), a high-order integrator for coupled differential equations, set to use backward differencing with Newton iteration. The ionization and heating/cooling source terms are integrated explicitly in the finite volume scheme, using an innovative algorithm that preserves the second-order time-accuracy of the numerical scheme and dramatically reduces the computation required for a given error tolerance (Mackey 2012).

### 3.7 RAMSES-LAMPRAY (TH, TF)

The radiative transfer module LAMPRAY (long characteristics AMR Parallel RAY tracing) is implemented into a derivative of the RAMSES cosmological code (Teyssier 2002; Fromang, Hennebelle & Teyssier 2006), which has been adapted to the detailed study of star formation. The code solves the MHD equations on a fully threaded tree (FTT) with support for self-gravity. Important additional physics modules compared to the original RAMSES code include accreting sink particles, coupling to the astrochemistry framework KROME, and many smaller changes to improve the stability and quality of the HLLD MHD solver in the case of supersonic flows. For the D-type test, the hydrodynamics is solved using a second-order MUSCL scheme with an HLLD solver and an isotropic monotonized central slope limiter.

The radiative transfer module employs ray tracing directly on the adaptive mesh. These are long characteristics rays covering the entire computational domain. The technique is made computationally feasible by, in addition to the FTT, also using a separate ray-oriented domain decomposition, in which the radiative transfer problem can be solved efficiently in parallel. A photon-conserving second-order accurate Triangular Shaped Cloud (TSC) interpolation between the two domains is used to calculate densities and abundances along the ray, and deposit the ionization and heating rates. The ionization solver is based on the C$^2$-RAY method Mellema et al. (2006a). In a given time-step first the ray geometry is established and the MPI and sorting keys are set up linking effectively cell centres with points along the ray. Then the rates in the time-step are found using an iterative method, that repeatedly computes the average ionization rate and the corresponding changes in abundance, until the two converge. The result is that in principle arbitrarily large time-steps can be taken, and the method is only limited by the Courant condition imposed by the fluid dynamics.

The ray scheme allows for a completely arbitrary placement of rays, and only domains that actually intersect with rays store knowledge about them, making the method scalable to thousands of cores. The flexible placement of rays in addition makes it possible to use a mixture of rays and solve simultaneously for the diffuse and point-source components of the radiation field.

### 3.8 RAMSES-RT (SG and JR)

RAMSES-RT[5] (Rosdahl et al. 2013) is a radiation-hydrodynamical extension of the RAMSES cosmological code. RAMSES (Teyssier 2002) solves the equations of gravitational-hydrodynamics with a second-order unsplit Godunov solver on an adaptive mesh, using a FTT structure. In this paper, the hydro-solver specified by Toro, Spruce & Speares (1994) has been adopted. The code is fully (MPI) parallel.

In RAMSES-RT, RT is integrated into the structural framework of RAMSES and coupled to the hydrodynamics via interactions with hydrogen and helium. The RT is solved on the adaptive mesh refinement (AMR) grid with a first-order moment method using the M1 closure for the Eddington tensor. This strategy has the advantages that the computational load is invariant with the number of radiation sources (moment method) and the radiation transport solver is local in space (M1 closure), i.e. it requires no information outside the local volume when advecting the photon fluid between cells.

The radiation-thermochemistry of hydrogen and helium is solved in RAMSES-RT assuming non-equilibrium, where the ionized fractions of those species are tracked explicitly as passive scalars that are advected with the gas flow.

For adaptability of the code, and because the implementation is designed in large part to simulate galactic and extragalactic scales, where radiation sources are highly dynamic, the radiation is advected with an explicit solver, which is subject to a Courant condition for the time-step. The solution to overcoming the extremely small implied time-step is to use the so-called reduced speed of light approximation (Gnedin & Abel 2001): the speed of light is simply slowed down by some factor, typically two or three orders of magnitude, such that the hydrodynamical time-step length is roughly maintained. In the RAMSES-RT tests described here, we reduce the speed of light by a factor $10^{-2}$ compared to the real value.

### 3.9 SEDNA (RK)

The ionization module named SEDNA is currently under development by Rolf Kuiper. The module is coupled to the static grid version of the open source MHD code PLUTO (Mignone et al. 2007). Up to now, the module works with static, rectangular, uniform and non-uniform grids in 1D–3D Cartesian, cylindrical, and spherical coordinates.

Similar to the hybrid radiation transport solver, introduced in Kuiper et al. (2010a) and Kuiper & Klessen (2013), the total ionizing radiation field is split into a direct ionization component and a diffuse radiation field. The ionization by direct irradiation from either a point source at the centre of the spherical domain or a plane parallel flux in Cartesian geometry is computed by a ray-tracing step along the first coordinate axis. For the secondary radiation

---

[5] The RAMSES-RT implementation is publicly available, as a part of the RAMSES code (https://bitbucket.org/rteyssie/ramses).

field, the module can either make use of the so-called 'on-the-spot' approximation, or the ionization of EUV photons created by direct recombination into the ground state can be computed using the flux-limited diffusion approximation. Ongoing development of the module is based on the numerical code descriptions by Yorke & Welz (1996) and Richling & Yorke (1997, 2000) as well as the lecture course material in Kudritzki, Yorke & Frisch (1988). The ionization module SEDNA can be coupled to the radiation transport solver mentioned above to allow the determination of gas and dust temperature in dusty ionized and non-ionized regions, respectively. Future development might include dust scattering and Far ultraviolet radiation fields, which contribute to the photoheating of gas as well as to carbon ionization.

The main purpose of the ionization module SEDNA will be its application in modelling the formation and feedback of massive (proto-)stars. In this sense, the module comprises an extension to previous numerical studies regarding radiation pressure (Kuiper et al. 2010b, 2011, 2012; Kuiper & Yorke 2013a), stellar evolution (Kuiper & Yorke 2013b), and protostellar outflow feedback (Kuiper, Yorke & Turner 2015).

## 3.10 SEREN (DH and TGB)

SEREN (Hubber et al. 2011) is an SPH code designed for star formation, planet formation and star cluster problems. SEREN uses a conservative 'grad-h' SPH implementation to model the hydrodynamics, a Barnes-Hut tree to model self-gravity, sink particles to model accretion on to protostars and several algorithms to model protostellar and stellar feedback (i.e. Stamatellos, Whitworth & Hubber 2012).

Bisbas et al. (2009) used the HEALPIX algorithm (Górski et al. 2005) to tessellate all surrounding directions into discrete vectors of equal solid angle that cover the whole surface. In that method, ionizing radiation is propagated along each HEALPIX ray, calculating the position of the ionization front and assuming ionization equilibrium and neglecting the diffuse field. The trapezium method is used to calculate the density at various 'evaluation points' along the ray following the radiation. The distance to the next evaluation point is given by $\Delta r = f_1 h$ where $f_1$ is a dimensionless constant of order unity and $h$ is the smoothing length calculated at the previous evaluation point. At the final evaluation point, a bisection method is used to accurately determine the location of the final ionization front. The temperature of particles is smoothed around the ionization front to prevent the two fluids (hot and cold) from becoming separated and forming a gap (e.g. see Price 2008). The angular resolution of the ionizing radiation can be refined at any point by splitting a ray into four child rays, which then compute the rest of the ionization integral independently. A ray is split when the width of the ray cone exceeds some fraction of the local smoothing length. This matches the ray resolution to the gas particle resolution.

SEREN now contains an updated version of this algorithm with two main improvements and optimizations.

(i) When creating the HEALPIX tessellation, the particles are divided into linked lists along each ray. When the rays are split to improve the resolution, the linked lists are also split along each ray amongst the four child rays. When the radiation is propagated along each ray, the step-size between evaluation points is taken as the minimum of the smoothing lengths between the previous and next particles. This ensures that the next evaluation point does not 'overshoot' if there is suddenly a dense region such as a high-density clump or a shock. This means the bisection iteration to find the ionization front is now performed more accurately with fewer steps.

(ii) When walking along the linked lists, if the previous and next particles have very similar properties to within some tolerance, then the density can be extrapolated from the particles rather than performing another (expensive) tree-walk. This speeds up the calculation, depending on the chosen tolerance.

Both of these optimizations lead to faster run times and a more accurate determination of the location of the ionization front. For roughly uniform density distributions, both methods give the same results. For strong density contrasts, particularly near the ionization front (which can be common later in the simulation), the results may diverge due to the different accuracies of finding the ionization front position. We perform all ionization tests using the latter implementation only.

## 3.11 TORUS (TJH)

TORUS is principally an AMR Monte Carlo radiation transport code capable of continuum, atomic line, non-Local Thermodynamical Equilibrium molecular line radiation transport (e.g. Harries 2000; Kurosawa, Harries & Symington 2006; Rundle et al. 2010) and most recently coupled radiation transport and photodissociation region chemistry (Bisbas et al. 2015). It was developed to treat radiation hydrodynamics problems using operator split photoionization and hydrodynamics by Haworth & Harries (2012) as follows.

TORUS uses a flux conserving, finite difference, total variation diminishing hydrodynamics scheme. It uses the Superbee flux limiter (Roe 1985) and includes a Rhie–Chow interpolation scheme to prevent odd–even decoupling (Rhie & Chow 1983).

Monte Carlo photoionization solves for the time-averaged energy density d$U$ in each cell by propagating constant-energy $\epsilon$ packets of photons over the computational grid and counting their path lengths $l$ through each cell of volume $V$

$$\mathrm{d}U = \frac{4\pi J_\nu}{c} \mathrm{d}\nu = \frac{\epsilon}{c\Delta t} \frac{1}{V} \sum_{\mathrm{d}\nu} l, \tag{20}$$

where $\epsilon$ is the total source luminosity divided by the number of photon packets used.

The estimated energy densities are used in the photoionization equilibrium equation (Osterbrock 1989) to solve for the ionization balance, which in terms of Monte Carlo estimators is

$$\frac{n(X^{i+1})}{n(X^i)} = \frac{\epsilon}{\Delta t V \alpha(X^i) n_e} \sum \frac{l \bar{\sigma}_\nu(X^i)}{h\nu}, \tag{21}$$

where $n(X^i)$, $\alpha(X^i)$, $\bar{\sigma}_\nu(X^i)$ and $n_e$ are the number density, recombination coefficient and absorption cross-section of ion $X^i$ and the electron density, respectively. The ionization fraction yields the temperature and therefore pressure under the simple thermal prescription used in this paper. To remain consistent with the other codes the on-the-spot approximation is employed by terminating the propagation of a photon packet after its first absorption and by using the case B recombination coefficient. Using operator splitting, hydrodynamics and photoionization calculations are performed sequentially until the simulation end time. The advantage of this approach is that many complex features usually only treated by dedicated radiation transport codes can be included in radiation hydrodynamics applications (e.g. the diffuse radiation field; Haworth & Harries 2012). The disadvantage is that it is computationally expensive, but this is overcome owing to the efficient parallelization of Monte Carlo radiation transport (Harries 2015).

## 4 THE D-TYPE BENCHMARK TEST

### 4.1 Initial physical conditions

For the purposes of the test we will use a simplified isothermal equation of state for both the ionized and the neutral medium. The treatment of the interface where the two media meet is left to each numerical method. The test is purely hydrodynamical, i.e. it includes no gravity or magnetic fields. Due to the nature of equation (8) we will run two tests: (i) to examine the early phase of the D-type expansion, i.e. where the Spitzer approximation (equation 9) is applicable and (ii) to examine the later phase of the D-type expansion, i.e. where the Raga expression (equation 8) is applicable.

In both early- and late-phase tests, we consider a uniform region containing pure hydrogen and an ionizing source emitting $\dot{\mathcal{N}}_{\mathrm{LyC}} = 10^{49}$ photons per second placed at the origin. The position of the source defines the origin of a Cartesian coordinate system. The density of the gas (hydrogen only) is taken to be $\rho_{\mathrm{o}} = 5.21 \times 10^{-21}\,\mathrm{g\,cm^{-3}}$. The temperature and the sound speed of the ionized gas are taken to be $T_{\mathrm{i}} = 10^4\,\mathrm{K}$ and $c_{\mathrm{i}} = 12.85\,\mathrm{km\,s^{-1}}$, respectively.

#### 4.1.1 Early phase

For the early phase expansion test the temperature of the neutral gas is initialized to $T_{\mathrm{o}} = 10^2\,\mathrm{K}$ corresponding to a sound speed of $c_{\mathrm{o}} = 0.91\,\mathrm{km\,s^{-1}}$. For the SPH calculations, we assume the dense gas takes the form of a cloud of finite radius, with total mass of $M_{\mathrm{cl}} = 640\,\mathrm{M_\odot}$. The radius of the cloud is therefore $R_{\mathrm{cl}} = 1.257\,\mathrm{pc}$, or $R_{\mathrm{cl}} = 4R_{\mathrm{St}}$. We evolve the simulation until $t_{\mathrm{end}} = 0.141\,\mathrm{Myr}$. At this time the ionization front has reached the edge of the domain (or the cloud in the SPH runs). The upper panel of Fig. 1 plots the analytical equations described in Section 2 for the early-phase expansion.

#### 4.1.2 Late phase

Equation (14) gives the stagnation radius as a function of the initial Strömgren radius.

$$R_{\mathrm{STAG}} = \left(\frac{c_{\mathrm{i}}}{c_{\mathrm{o}}}\right)^{4/3} R_{\mathrm{St}}, \qquad (22)$$

As we discuss in Section 4.2.1, the number of SPH particles required for the late-phase test may lead to prohibitively high computational expenses (see equation 27 in particular where there is a dependence on $(\frac{c_{\mathrm{i}}}{c_{\mathrm{o}}})^4$). We will therefore adopt a 'neutral' temperature of $T_{\mathrm{o}} = 10^3\,\mathrm{K}$ while keeping $\mu_{\mathrm{o}} = 1$. The corresponding sound speed is then $c_{\mathrm{o}} = 2.87\,\mathrm{km\,s^{-1}}$. As for the early-phase calculations, the initial Strömgren radius is $R_{\mathrm{St}} = 0.314\,\mathrm{pc}$. The stagnation radius $R_{\mathrm{STAG}} = 2.31\,\mathrm{pc}$ is obtained at $t_{\mathrm{STAG}} \simeq 3.0\,\mathrm{Myr}$ which defines the time we terminate the simulation.

For the late-phase SPH calculations, the cloud has mass $M_{\mathrm{cl}} = 8 \times 10^3\,\mathrm{M_\odot}$ and $R_{\mathrm{cl}} = 2.91\,\mathrm{pc}$. The lower panel of Fig. 1 plots the analytical equations described in Section 2 for the late-phase expansion.

### 4.2 Numerical setup and configuration

#### 4.2.1 SPH setup

We choose a slightly bigger cloud radius than the stagnation radius to avoid the effect of an expanding shell in vacuum when $t = t_{\mathrm{STAG}}$.
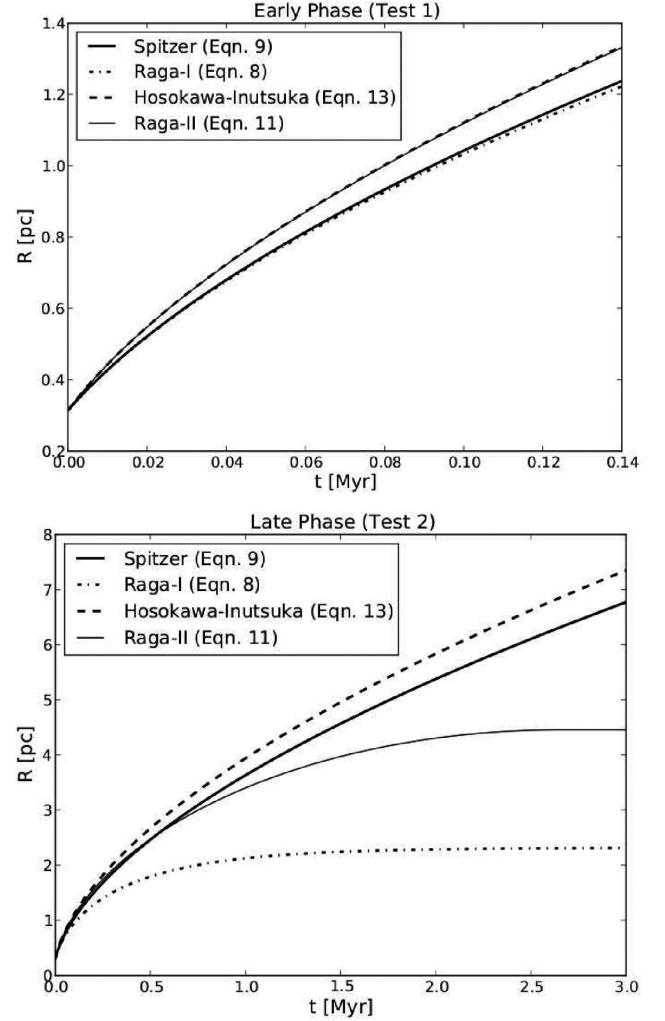


**Figure 1.** Analytical expressions of equations (8) (Raga-I), (11) (Raga-II), (9) (Spitzer), and (13) (Hosokawa–Inutsuka) for the 'early phase' (upper panel) and for the 'late phase' tests. The x-axis is the time (Myr) and the y-axis the position of fronts (pc).

Let $g$ be this additional factor determining the extra size of the cloud radius,

$$R_{\mathrm{cl}} = g R_{\mathrm{STAG}} \qquad (23)$$

and let $f \equiv g \left(\frac{c_{\mathrm{i}}}{c_{\mathrm{o}}}\right)^{4/3}$.

Suppose that $R_{\mathrm{cl}} = f R_{\mathrm{St}}$, where $R_{\mathrm{cl}}$ is the radius of the spherical cloud, $R_{\mathrm{St}}$ is the Strömgren radius and $f > 1$ is a user-defined factor. $f$ describes the size of the Strömgren sphere in comparison with the size of the spherical cloud.

The density at $t = 0$ is homogeneous throughout the cloud. Therefore,

$$\rho_{\mathrm{o}} = \frac{f^3 \dot{\mathcal{N}}_{\mathrm{LyC}} m^2}{M_{\mathrm{cl}} \alpha_{\mathrm{B}}}. \qquad (24)$$

Let $N_{\mathrm{SPH}}^{\mathrm{St}}$ be the number of SPH particles consisting the Strömgren sphere. All SPH particles have the same mass, $m_{\mathrm{SPH}}$. Then

$$\rho_{\mathrm{o}} = \frac{3M_{\mathrm{St}}}{4\pi R_{\mathrm{St}}^3} = \frac{3N_{\mathrm{SPH}}^{\mathrm{St}} m_{\mathrm{SPH}}}{4\pi R_{\mathrm{St}}^3} \qquad (25)$$

and

$$\rho_o = \frac{3M_{cl}}{4\pi R_{cl}^3} = \frac{3N_{SPH}^{cl} m_{SPH}}{4\pi R_{cl}^3}. \tag{26}$$

Combining the above, we obtain $N_{SPH}^{cl} = f^3 N_{SPH}^{St}$. This equation gives the total number of SPH particles for a specific size and resolution of the Strömgren sphere. In all cases we will use a pre-settled particle distribution, i.e. a 'glass' structure, which minimizes (but does not eliminate) the numerical noise.

For the test examining the early phase we will use $f = 4$ and $N_{SPH}^{St} = 10^4$. Therefore the total number of SPH particles is taken to be $N_{SPH}^{cl} = 6.4 \times 10^5$ particles. We also use $m_{SPH} = 10^{-3}\,M_{\odot}$, which therefore implies $M_{cl} = 640\,M_{\odot}$.

For the test examining the late phase, the total number of SPH particles is

$$N_{SPH}^{cl} = g^3 \left(\frac{c_i}{c_o}\right)^4 N_{SPH}^{St}. \tag{27}$$

Using $g = 1.26$ (because at this value $g^3 \simeq 2$) and $N_{SPH}^{St} = 10^4$ we obtain a total of $N_{SPH}^{cl} = 8 \times 10^6$ SPH particles, each one having mass $m_{SPH} = 10^{-3}\,M_{\odot}$.

### 4.2.2 3D grid setup

The radiation source is placed at the origin, as before. The three-dimensional Eulerian calculations are run for a single octant with a spatial resolution of $128^3$ grid zones. Reflecting boundary conditions are used in the negative directions, and zero gradient boundary conditions in the positive directions. An octant runs from $\{x, y, z\} \in [0, 3.874 \times 10^{18}]$ cm, corresponding to $4R_{St}$ ($R_{St} = 0.9685 \times 10^{18}$ cm $= 0.314$ pc).

For the late-phase test the simulation was set up in a similar way, but with the simulation domain now extending to $1.26\,R_{STAG} = 2.91$ pc to agree with the SPH setup (Sec. 4.2.1). The ISM density is the same, but the neutral gas temperature is initialized to $10^3$ K instead of $10^2$ K, so the pressure ratio between ionized and neutral gas is reduced to 20 in the initial conditions.

### 4.2.3 1D simulations

For 1D simulations, contributors were encouraged to use any algorithm available for solving spherically symmetric problems. The simulation domain was typically set to a somewhat larger value than $4R_{St}$ so that the shock front remained inside the grid until the finishing time of the simulation. For the early-phase test, a maximum radius of 1.5 pc was sufficient, while for the late-phase test the maximum radius was taken to be 5 pc. Numerical schemes used include a uniform grid (PION, SEDNA, HERACLES, TORUS), adaptive Eulerian mesh (AQUILINE), and a Lagrangian mesh (GLIDE). The different schemes resulted in a significant range of spatial resolutions from code to code.

## 5  RESULTS

### 5.1  1D runs

#### 5.1.1 Early-phase test (Test 1-1D)

The six 1D hydrodynamical codes use a variety of grids specified in Table 1. In these runs, a variety of resolutions have been studied. Where practicable, runs were performed at increasing resolution

**Table 2.** Number of cells used by the 1D participating codes for both early- and late-phase tests (Test 1-1D and Test 2-1D, respectively).

| Code name | No. grid cells |
|---|---|
| AQUILINE | 32 768 |
| GLIDE | 378 |
| HERACLES | 16 834 |
| PION | 131 072 |
| SEDNA | 16 834 |
| TORUS | 1024 |

until the results converged and the resolution requirements turned out to be different for different codes. In this section, we show only the highest resolution results, in order to provide a validated reference solution to which other results may be compared (see Table 2 for the resolution each 1D code used).

Fig. 2 shows the density as a function radius for the six 1D codes participating in the Test 1-1D. In this figure, we plot four different evolutionary times, i.e. $t = 0.005$, 0.02, 0.08 and 0.14 Myr. We also indicate with vertical lines the position of the extent of the H II regions as predicted by the various approximations presented in Section 2. All codes agree very well with each other; the peak density and shell width vary between codes because of the different spatial resolutions used. At early times the position of the thin shell agrees with the Spitzer solution (equation 9) but then moves towards the Hosokawa–Inutsuka (equation 13) solution even overtaking it at late times. At $t = 0.08$ and 0.14 Myr it is clear that equation (9) no longer correctly describes the evolution. At this stage all codes at least partially resolve the shell width.

The two panels in Fig. 3 show the position of the ionization front, defined as the position at which $x_i = 0.5$, compared to the Spitzer (equation 9) and the Hosokawa–Inutsuka (equation 13) approximations. The lower panel shows the relative error of each code as compared to those two analytical approximations. This relative error is ~8 per cent for the Spitzer and $\lesssim 1$ per cent for the Hosokawa–Inutsuka approximation at $t \gtrsim 0.08$ Myr, and so we conclude that all participating codes agree with the Hosokawa–Inutsuka approximation and none with the Spitzer formulation at this level of accuracy.

In Table 3 we show (columns 2 and 4, respectively) the mean position of the ionization front $\langle R_{IF} \rangle$ at several times and the standard deviation, $\sigma$, as obtained by the six different 1D codes. We find that the position $r$ is remarkably similar between the codes, as the relative difference is $\lesssim 1$ per cent in all cases, and that this difference decreases with time. In the same table we show (in column 6) the mean maximum density reached, $\langle \rho_{max} \rangle$, as well as the respective standard deviation (in column 7). As before, better agreement is obtained as $t$ increases.

At later times, the H II region expansion slows down monotonically, and so in reality the shock Mach number (hence compression factor and maximum density) also decreases monotonically. The shell mass and thickness also increase monotonically with time as more mass is swept up. This means that the quoted $\langle \rho_{max} \rangle$ is certainly an underestimate compared to the analytic solution at early times, and gradually reaches the correct value at later times. This can be seen in the first panel of Fig. 2, where all of the codes have different peak densities because of the differing spatial resolution. The largest density achieved (by GLIDE) is significantly larger than the mean value quoted in Table 3.
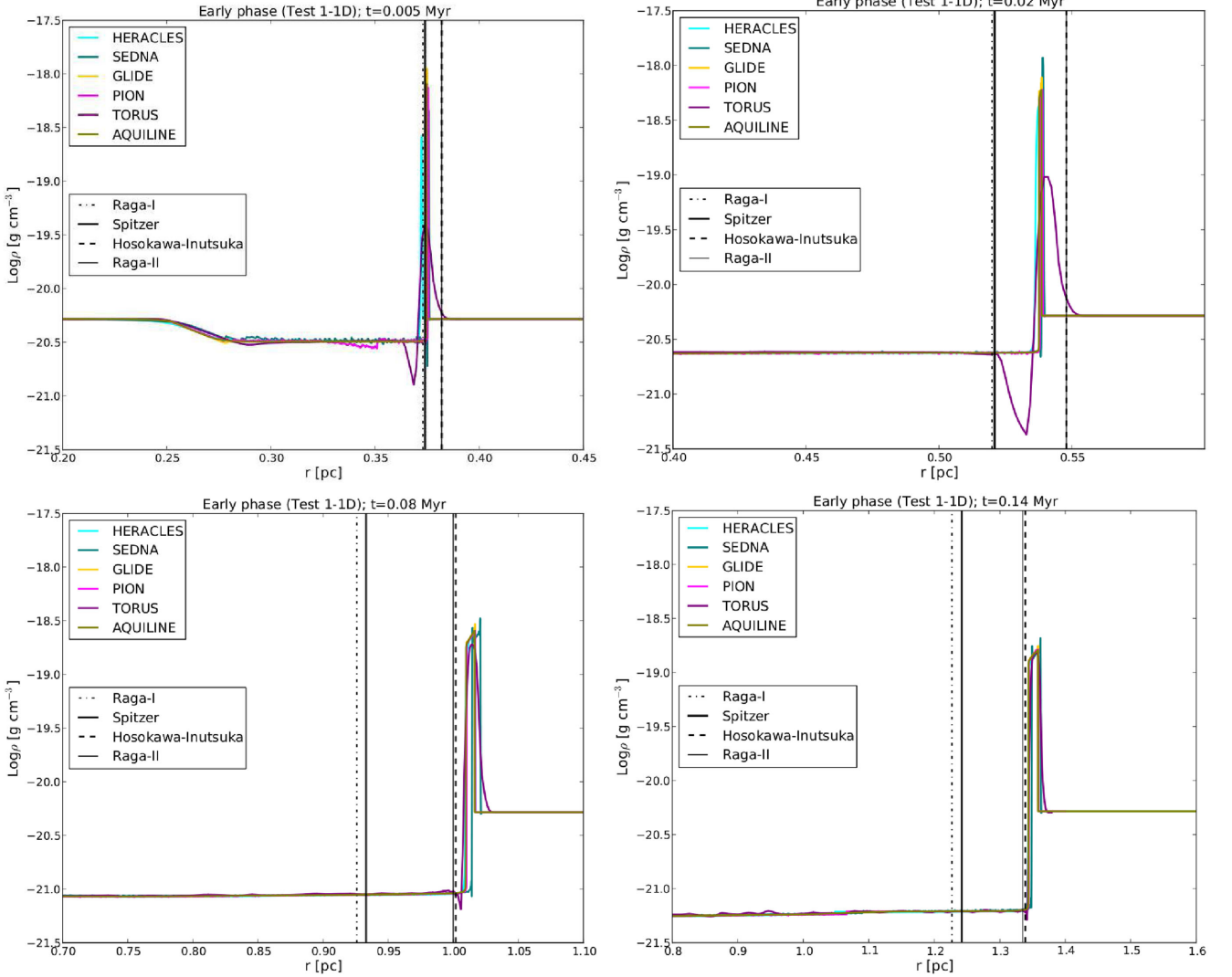
**Figure 2.** Density plots of the 1D codes for the early-phase test. The panels correspond to different evolutionary times. The *x*-axis in these panels is the distance from the ionizing source (pc) and the *y*-axis is the density (g cm$^{-3}$). We plot snapshots at $t = 0.005$ Myr (top left), $t = 0.02$ Myr (top right), $t = 0.08$ Myr (middle left), and $t = 0.14$ Myr (middle right). We find very good agreement between all codes. We see that at $t = 0.005$ Myr the codes reproduce the position predicted by the Spitzer equation (equation 9), whereas at the end of the simulation, $t = 0.14$ Myr, the maximum density is located further than the Hosokawa–Inutsuka equation (equation 13). Further details are discussed in Section 5.1.1

### 5.1.2 Late-phase test (Test 2-1D)

Fig. 4 shows the density as a function of radius for the six participating 1D codes in the Test 2-1D for different times, i.e. $t = 0.05$, 0.2, 0.8 and 3.0 Myr. The vertical lines correspond to the positions predicted by the analytical expressions discussed in Section 2. Table 4 gives the mean position of the ionization front with the standard deviation (columns 2 and 4) as well as the mean and standard deviation for the maximum density reached (columns 6 and 7). The relative difference around $\langle R_{\rm IF} \rangle$ is $\lesssim 2$ per cent in all cases.

In this late-phase test, the position of the ionization front stagnates as predicted by equation (8) (Raga-I) since the H II region is in pressure equilibrium with the pressure of the neutral medium. Indeed, as shown in Table 4, the mean stagnation radius (measured at $t = 3.0$ Myr) as given by all six participating codes is $\langle R_{\rm IF} \rangle = 2.359$ pc (standard

deviation $\sigma = 0.032$ pc or $\sim 1.3$ per cent from this mean value) which gives a relative error of $\sim 2.2$ per cent when compared to equation (14).

The shell thickness is a function of resolution, which is why the thickness obtained by TORUS is larger than the other results (i.e. 1024 cells, compared to a maximum of 40 960 used in PION). The shell develops rapidly and becomes geometrically thick by $t = 0.05$ Myr. As seen in Fig. 4, the thickness is remarkably similar as calculated by all six participating codes. The shell becomes thicker over time as observed for $t \geq 0.2$ Myr. The leading shock eventually becomes a detached expanding compression wave, and the value of the maximum density $\rho_{\rm max}$ drops down towards $\sim \rho_{\rm o}$ which is the density of the undisturbed neutral medium (i.e. at the beginning of each simulation).

Fig. 5 shows the position of the ionization front of all codes compared with equations (8) (Raga-I) and (11) (Raga-II). For reference, we also plot the Spitzer and Hosokawa–Inutsuka equations. As first
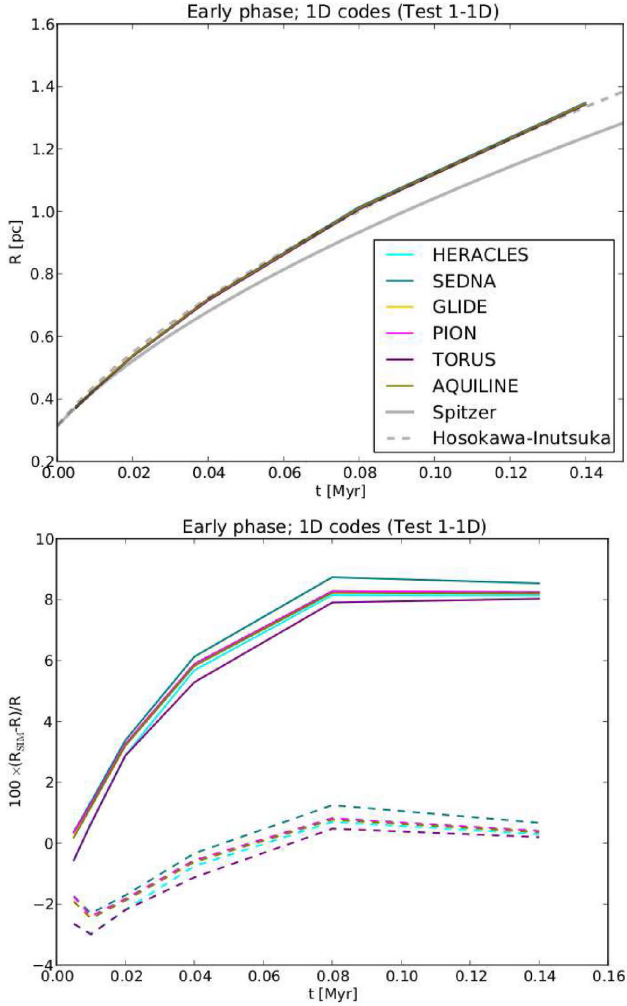
**Figure 3.** Position at which the ionization fraction is $x_i = 0.5$ as calculated by the 1D participating codes. The upper panel compares the codes with the Spitzer (equation 9; solid grey line) and the Hosokawa–Inutsuka (equation 13; dashed grey line) equations. The lower panel shows the relative error found between the numerical solution and either of the two analytical equations (solid lines correspond to the errors due to the comparison with the Spitzer equation, while dashed lines due to the Hosokawa–Inutsuka equation).

**Table 3.** This table shows results from the 'early phase' test (see Section 5.1.1). Column 1 shows the time. Columns 2 and 4 show the mean position of the ionization front, $\langle R_{IF} \rangle$ with the corresponding standard deviation, $\sigma$, for 1D codes. Columns 3 and 5 are the respective for 3D codes. Columns 6 and 7 show the mean maximum density of the shock front $\langle \rho_{max} \rangle$ and its standard deviation, $\sigma$, for 1D codes only.

| $t$ (Myr) | $\langle R_{IF} \rangle$ (pc) | | $\sigma/10^{-3}$ (pc) | | $\langle \rho_{max} \rangle/10^{-19}$ (g cm$^{-3}$) | $\sigma/10^{-19}$ (g cm$^{-3}$) |
|---|---|---|---|---|---|---|
| | 1D | 3D | 1D | 3D | 1D | 1D |
| 0.005 | 0.373 | 0.378 | 2.059 | 2.76 | 5.7 | 3.6 |
| 0.01 | 0.430 | 0.430 | 3.180 | 2.96 | 5.9 | 3.0 |
| 0.02 | 0.536 | 0.530 | 2.488 | 3.26 | 6.1 | 3.3 |
| 0.04 | 0.717 | 0.707 | 3.848 | 3.59 | 4.2 | 1.4 |
| 0.08 | 1.009 | 0.996 | 3.679 | 4.35 | 2.6 | 0.4 |
| 0.14 | 1.343 | 1.324 | 2.848 | 4.29 | 1.7 | 0.2 |

shown by Raga et al. (2012a), the codes initially follow the position predicted by equation (11), however they 'relax' towards the stagnation radius expected from pressure balance predicted by equation (14). The position of the ionization front temporarily expands beyond the stagnation radius before relaxing inwards. According to Raga et al. (2012a), this 'overshoot' is due to the inertia of the H II region.

Here, we provide a semi-empirical equation (which we call the 'STARBENCH equation') predicting the position of the ionization front for this late phase test for $t \in [0, 3]$ Myr. The STARBENCH equation has the form

$$R_{SB} = \mathcal{R}_{II} + f_{SB}(\mathcal{R}_I - \mathcal{R}_{II}), \tag{28}$$

where $\mathcal{R}_I$ and $\mathcal{R}_{II}$ are the numerical solutions of equations (8) and (11), respectively, and $f_{SB}$ is assumed to be a time-dependent dimensionless factor. For the purposes of this paper we approximate $f_{SB}$ with the following form

$$f_{SB} = 1 - A \exp\left[-\frac{t}{\text{Myr}}\right], \tag{29}$$

where $A = 0.733$. This equation is plotted in Figs 5 and 7 and shows very good agreement with all 1D and 3D simulations. We propose that coders who benchmark their algorithm against this late phase test should use equations (8), (11), (28), and (29) with the indicated constant for $t \gtrsim 0.05$ Myr.

### 5.1.3 Summary of 1D results

Overall we find good agreement between all six 1D participating codes. In order to achieve this we require such a high resolution that a 3D calculation would be prohibitively expensive ($\gg 10^4$ cells in each dimension for a uniform grid, see also Bisbas et al. 2009, for the relevant discussion in SPH). Although all codes are in excellent agreement at sufficiently fine mesh scales, we find limited agreement with the existing and widely used analytic forms. We attribute this to the approximations made in deriving these analytic forms. Many of these approximations are only valid when applied to the early phase thin shell expansion. We provide a tuned fitting formula for which all codes mutually agree to $\lesssim 0.5$ per cent error at all times.

### 5.2 3D runs

#### 5.2.1 Early-phase test (Test 1-3D)

In Appendix A, we present (Figs A4 and A5) snapshots of slices through the density distributions at various times during the evolution of the H II region for the eight 3D participating codes. In general, the agreement in structure and front position between the widely different codes is excellent.

There are, however, some significant differences. At $t = 0.005$ Myr, the peak density of the shell as simulated by the SPH code SEREN is significantly lower than the other codes and the shell is broader. However, the agreement improves at later times. If the number of SPH particles is increased, this leads to a better agreement suggesting that a higher particle count is required to achieve comparable resolution to the grid-based codes. The number of SPH particles used was tuned to match the overall expansion of the H II region (i.e. $10^4$ particles for the initial Strömgren sphere) rather than to resolve the shell structure. However, the total particle count ($6.4 \times 10^5$) is comparable to the number of zones in the Eulerian calculations ($128^3$).
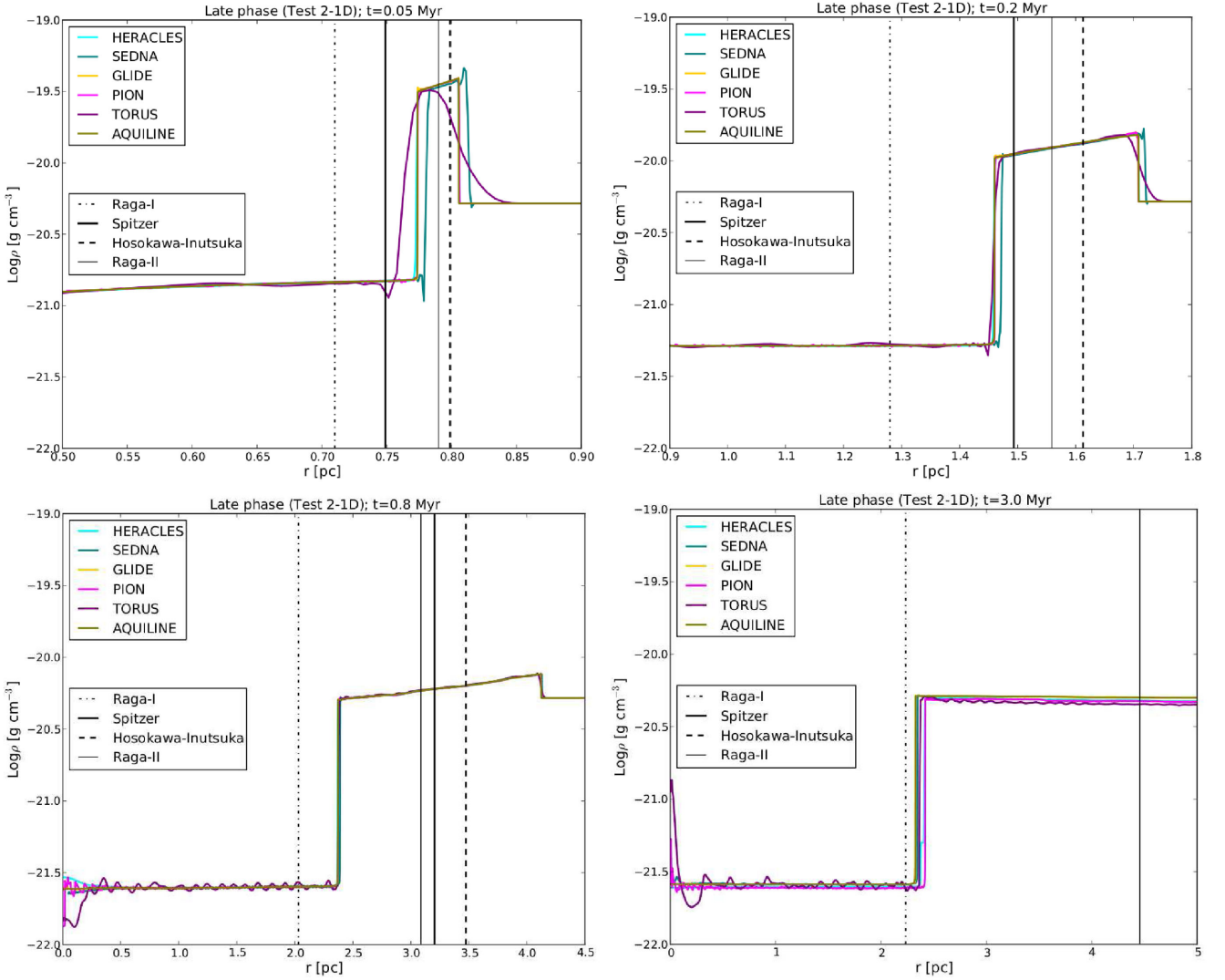
**Figure 4.** As in Fig. 2 for the late-phase test. We plot snapshots at $t = 0.05$ Myr (top left), $t = 0.2$ Myr (top right), $t = 0.8$ Myr (middle left), and $t = 3.0$ Myr (middle right).

As time progresses, evidence of instability appears in some of the calculations. In particular, the instabilities are particularly prominent in FLASH-TREERAY and CAPREOLE-C$^2$-RAY, which both use the PPM algorithm to steepen discontinuities. It should be mentioned here that in these particular cases the instabilities develop first in the places where the shock in the neutral gas is propagating parallel to the grid and that if a different cut through the 3D data cube is taken, the instabilities are not in evidence. This strongly suggests that for these two codes the instability is of the odd–even type, first described by Quirk (1994). These stabilities can be cured by introducing extra numerical diffusion into the PPM scheme when a strong shock is detected parallel to the grid direction, or using a hybrid Riemann solver, which switches from the usual Riemann solver (e.g. the Roe solver used by CAPREOLE-C$^2$-RAY) to a more diffusive Riemann solver such as an HLLE solver, inside shocks.

Fig. 6 shows the comparison of the analytical equations, as we discussed above, to the eight participating 3D codes. Here, we find that all codes also follow the expansion law as expressed by the Hosokawa–Inutsuka equation (13), with error $\lesssim 4$ per cent

**Table 4.** As in Table 3 for the 'late phase' test.

| $t$ (Myr) | $\langle R_{IF} \rangle$ (pc) | | $\sigma / 10^{-3}$ (pc) | | $\langle \rho_{max} \rangle / 10^{-20}$ (g cm$^{-3}$) | $\sigma / 10^{-21}$ (g cm$^{-3}$) |
|------|-------|-------|-------|-------|------|------|
| | 1D | 3D | 1D | 3D | 1D | 1D |
| 0.05 | 0.771 | 0.733 | 8.685 | 2.606 | 3.90 | 4.0 |
| 0.1 | 1.063 | 1.025 | 4.356 | 2.741 | 2.43 | 1.8 |
| 0.2 | 1.460 | 1.420 | 6.772 | 2.645 | 1.57 | 0.5 |
| 0.4 | 1.934 | – | 6.366 | – | 1.05 | 0.4 |
| 0.8 | 2.375 | 2.349 | 7.450 | 6.739 | 0.73 | 0.8 |
| 1.6 | 2.515 | 2.506 | 10.07 | 5.854 | 0.58 | 0.6 |
| 3.0 | 2.359 | 2.424 | 31.71 | 1.534 | 0.53 | 0.3 |

at $t \gtrsim 0.08$ Myr in contrast to $\gtrsim 5$ per cent when compared to the Spitzer equation (9). Table 3 shows the mean position, $\langle R_{IF} \rangle$ (column 3), of the ionization front and the standard deviation (column 5) for all these codes which we find to agree to within 3–7 per cent around $\langle R_{IF} \rangle$. As noted earlier, all codes agree with the Spitzer approximation only for $t \lesssim 0.07$ Myr, however based
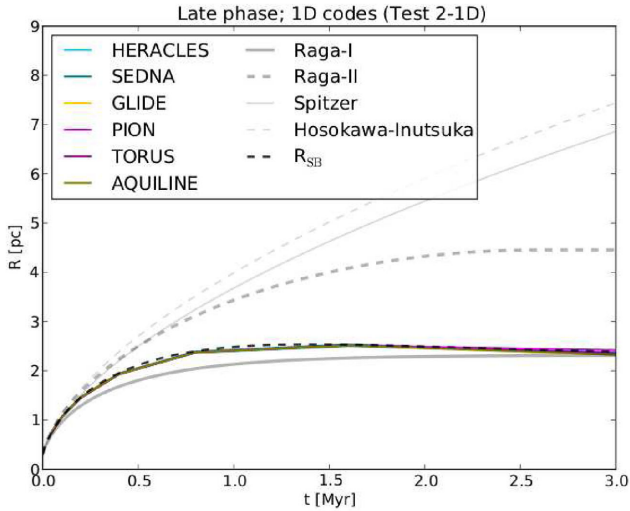
**Figure 5.** Comparison between equations (8) (Raga-I), and (11) (Raga-II) for the 1D participating codes. The black dashed line corresponds to the STAR-BENCH equation (28). We additionally plot the Spitzer and the Hosokawa–Inutsuka (HI) expansion laws for reference.





**Figure 6.** As in Fig. 3 for the 3D participating codes.



**Figure 7.** As in Fig. 5 for the 3D participating codes.

on the 1D simulations, we argue that this value of time will be decreased down to $\sim 0.01$ Myr by increasing the resolution substantially.

### 5.2.2 Late-phase test (Test 2-3D)

Figs A4 and A5 show cross-section density plots at times $t = 0.05$, 0.2, 0.8, and $t = 3.0$ Myr. We find that all codes are in excellent qualitative agreement until $t \sim 0.8$ Myr. From $t \approx 0.8$ Myr, most of the codes show some level of D-type instability similar to that shown in Williams (2002). This has the largest magnitude in PION, for which the resulting Reynolds stresses appear to be causing the ionization front to expand to a larger radius than found in the other codes.

In the case of the SPH code SEREN, the shell becomes prone to the tensile instability (Monaghan 2000) and it creates high-density contrast fluctuations in its interior. Eventually at $t = 3.0$ Myr the shell has been completely detached and the hot ionized medium is bounded by vacuum. One would expect that this ionized region would expand rapidly into the external vacuum as long as the shell is detached; however, it appears that because there are no SPH particles in this region the SPH summations do not sample it and hence the edge of the region functions as a smooth flow boundary condition. This may be a similar issue to the known contact discontinuity problem in SPH (Agertz et al. 2007; Price 2008).

Fig. 7 shows a comparison of the position of the ionization front as calculated by all participating 3D codes and the analytical solutions. We additionally plot the STARBENCH equation (28). As we explained in Section 5.2.1, none of the codes reproduce any of the analytical solutions. Table 4 shows the mean values of the distance of the ionization front and the corresponding standard deviation. All codes are in very good mutual agreement within $\lesssim 5$ per cent.

## 6 SUMMARY AND CONCLUSIONS

We have studied the standard radiation hydrodynamical test case of an H II region expanding in an initially uniform density medium. 12 distinct codes participated in this STARBENCH comparison test. We examined two scenarios of the initial 'early phase' expansion and the 'late phase' relaxation to pressure equilibrium with the external medium.

The early-phase test shows that the Hosokawa–Inutsuka approximation (equation 13) which results directly from the equation of motion of the expanding shell and which is in fact a second-order Ordinary Differential Equation (ODE), agrees with the numerical results. In contrast, the Spitzer approximation (equation 9) which results from the assumption that the thermal pressure of the H II region matches approximately with the ram pressure, and which is a first-order ODE, underestimates the numerical results by a small-but-significant factor ($\sim 8$ per cent), because it does not include the effect of the inertia of the material entrained in the shell.

In the late-phase test, we tested the codes against equations (8) (Raga-I) and (11) (Raga-II) which include the pressure of the undisturbed medium acting on the H II region and are generalizations of equations (9) (Spitzer) and (13) (Hosokawa–Inutsuka), respectively. With time, this pressure becomes approximately equal to the thermal pressure within the H II region, at which point the system reaches equilibrium and the expansion of the ionization front is halted. Our benchmarking test showed that all participating codes start by following the expansion law as expressed by equation (11) (Raga-II), while at later times the H II region stagnates at the position predicted by static pressure balance.

Since the codes do not agree with any of the analytic expressions, we have developed an analytic parametrization (which we call the 'STARBENCH equation') that describes the early- and late-phase expansion of an H II region to within $\lesssim 2$ per cent at all times which we recommend be used for future code validations, exercises and analytical studies of massive star-forming regions.

The structure of the expanding H II region is overall in very good agreement between all the contributing codes. We have discussed physics-related issues, such as instabilities, which apply in certain case and which may either be physical or numerical. This agreement between the codes has improved dramatically as result of the comparison test we present in this paper. This comparison has increased the confidence of the scientific robustness of the results of all participating codes.

## ACKNOWLEDGEMENTS

## REFERENCES

Agertz O. et al., 2007, MNRAS, 380, 963
Arthur S. J., Henney W. J., Mellema G., de Colle F., Vázquez-Semadeni E., 2011, MNRAS, 414, 1747
Audit E., González M., Vaytet N., Fromang S., Hennebelle P., Teyssier R., Tremblin P., Thooris B., 2011, Astrophysics Source Code Library, record ascl:1102.016
Axford W. I., 1961, Phil. Trans. R. Soc. A, 253, 301
Baczynski C., Glover S. C. O., Klessen R. S., 2015, preprint (arXiv:1503.08987)
Berger M. J., Colella P., 1989, J. Comput. Phys., 82, 64
Bertoldi F., 1989, ApJ, 346, 735
Bisbas T. G., Wünsch R., Whitworth A. P., Hubber D. A., 2009, A&A, 497, 649
Bisbas T. G., Wünsch R., Whitworth A. P., Hubber D. A., Walch S., 2011, ApJ, 736, 142
Bisbas T. G., Haworth T. J., Barlow M. J., Viti S., Harries T., Bell T. A., Yates J., 2015, MNRAS, submitted
Boneberg D. M., Dale J. E., Girichidis P., Ercolano B., 2015, MNRAS, 447, 1341
Cohen S. D., Hindmarsh A. C., Dubois P. F., 1996, Comput. Phys., 10, 138
Colella P., Woodward P. R., 1984, J. Comput. Phys., 54, 174
Colín P., Vázquez-Semadeni E., Gómez G. C., 2013, MNRAS, 435, 1701
Dale J. E., Bonnell I. A., Whitworth A. P., 2007, MNRAS, 375, 1291
Dale J. E., Ercolano B., Bonnell I. A., 2012, MNRAS, 424, 377
Dubey A., Reid L. B., Fisher R., 2008, Phys. Scr. T, 132, 014046
Dyson J. E., Williams D. A., 1980, The Physics of the Interstellar Medium. Manchester Univ. Press, Manchester.
Elmegreen B. G., Lada C. J., 1977, ApJ, 214, 725
Eulderink F., Mellema G., 1995, A&AS, 110, 587
Falle S. A. E. G., 1991, MNRAS, 250, 581
Falle S. A. E. G., Komissarov S. S., Joarder P., 1998, MNRAS, 297, 265
Fromang S., Hennebelle P., Teyssier R., 2006, A&A, 457, 371
Fryxell B. et al., 2000, ApJS, 131, 273
Gingold R. A., Monaghan J. J., 1977, MNRAS, 181, 375

Glover S. C. O., Clark P. C., 2012, MNRAS, 421, 9

Glover S. C. O., Mac Low M.-M., 2007a, ApJS, 169, 239

Glover S. C. O., Mac Low M.-M., 2007b, ApJ, 659, 1317

Glover S. C. O., Federrath C., Mac Low M.-M., Klessen R. S., 2010, MNRAS, 404, 2

Gnedin N. Y., Abel T., 2001, New Astron., 6, 437

González M., Audit E., Huynh P., 2007, A&A, 464, 429

Górski K. M., Hivon E., Banday A. J., Wandelt B. D., Hansen F. K., Reinecke M., Bartelmann M., 2005, ApJ, 622, 759

Gritschneder M., Naab T., Walch S., Burkert A., Heitsch F., 2009, ApJ, 694, L26

Harries T. J., 2000, MNRAS, 315, 722

Harries T. J., 2015, MNRAS, 448, 3156

Haworth T. J., Harries T. J., 2012, MNRAS, 420, 562

Henney W. J., Arthur S. J., de Colle F., Mellema G., 2009, MNRAS, 398, 157

Hosokawa T., Inutsuka S.-i., 2006, ApJ, 646, 240

Hubber D. A., Batty C. P., McLeod A., Whitworth A. P., 2011, A&A, 529, AA27

Iliev I. T. et al., 2006, MNRAS, 371, 1057

Iliev I. T. et al., 2009, MNRAS, 400, 1283

Kahn F. D., 1954, Bull. Astron. Inst. Neth., 12, 187

Kessel-Deynet O., Burkert A., 2003, MNRAS, 338, 545

Krumholz M. R., Stone J. M., Gardiner T. A., 2007, ApJ, 671, 518

Kudritzki R. P., Yorke H. W., Frisch H., 1988, 18th Saas-Fee Advanced Course Vol. 458, Radiation in Moving Gaseous Media. Springer-Verlag, Berlin, p. 89

Kuiper R., Klessen R. S., 2013, A&A, 555, AA7

Kuiper R., Yorke H. W., 2013a, ApJ, 763, 104

Kuiper R., Yorke H. W., 2013b, ApJ, 772, 61

Kuiper R., Klahr H., Dullemond C., Kley W., Henning T., 2010a, A&A, 511, 81

Kuiper R., Klahr H., Beuther H., Henning T., 2010b, ApJ, 722, 1556

Kuiper R., Klahr H., Beuther H., Henning T., 2011, ApJ, 732, 20

Kuiper R., Klahr H., Beuther H., Henning T., 2012, A&A, 537, AA122

Kuiper R., Yorke H. W., Turner N. J., 2015, ApJ, 800, 86

Kurosawa R., Harries T. J., Symington N. H., 2006, MNRAS, 370, 580

Lasker B. M., 1966, ApJ, 143, 700

Lefloch B., Lazareff B., 1994, A&A, 289, 559

LeVeque R. J., 2002, Finite Volume Methods for Hyperbolic Problems. Cambridge Univ. Press, Cambridge

Lucy L. B., 1977, AJ, 82, 1013

McKee C. F., van Buren D., Lazareff B., 1984, ApJ, 278, L115

Mackey J., 2012, A&A, 539, AA147

Mackey J., Lim A. J., 2010, MNRAS, 403, 714

Mackey J., Lim A. J., 2011, MNRAS, 412, 2079

Mathews W. G., 1965, ApJ, 142, 1120

Mathews W. G., O'Dell C. R., 1969, ARA&A, 7, 67

Matzner C. D., 2002, ApJ, 566, 302

Medina S.-N. X., Arthur S. J., Henney W. J., Mellema G., Gazol A., 2014, MNRAS, 445, 1797

Mellema G., Raga A. C., Canto J., Lundqvist P., Balick B., Steffen W., Noriega-Crespo A., 1998, A&A, 331, 335

Mellema G., Iliev I. T., Alvarez M. A., Shapiro P. R., 2006a, New Astron., 11, 374

Mellema G., Arthur S. J., Henney W. J., Iliev I. T., Shapiro P. R., 2006b, ApJ, 647, 397

Mignone A., Bodo G., Massaglia S., Matsakos T., Tesileanu O., Zanni C., Ferrari A., 2007, ApJS, 170, 228

Monaghan J. J., 2000, J. Comput. Phys., 159, 290

Osterbrock D. E., 1989, Research supported by the University of California, John Simon Guggenheim Memorial Foundation, University of Minnesota, et al. University Science Books, Mill Valley, CA

Péquignot D. et al., 2001, in Ferland G., Savin D. W., eds, ASP Conf. Ser. Vol. 247, Spectroscopic Challenges of Photoionized Plasmas. Astron. Soc. Pac., San Francisco, p. 533

Peters T., Banerjee R., Klessen R. S., Mac Low M-M., Galván-Madrid R., Keto E. R., 2010, ApJ, 711, 1017

Peters T., Banerjee R., Klessen R. S., Mac Low M.-M., 2011, ApJ, 729, 72

Price D. J., 2007, PASA, 24, 159

Price D. J., 2008, J. Comput. Phys., 227, 10040

Quirk J. J., 1994, Int. J. Numer. Methods Fluids, 18, 555

Raga A. C., Cantó J., Rodríguez L. F., 2012a, Rev. Mex. Astron. Astrofis., 48, 149

Raga A. C., Cantó J., Rodríguez L. F., 2012b, MNRAS, 419, L39

Rhie C. M., Chow W. L., 1983, AIAA J., 21, 1525

Richling S., Yorke H. W., 1997, A&A, 327, 317

Richling S., Yorke H. W., 2000, ApJ, 539, 258

Roe P. L., 1985, Proc. 15th Summer Seminar on Applied Mathematics, Large-Scale Computations in Fluid Mechanics. Am. Math. Soc., Providence, RI, p. 163

Roe P. L., 1986, Annu. Rev. Fluid Mech., 18, 337

Röllig M. et al., 2007, A&A, 467, 187

Rosdahl J., Blaizot J., Aubert D., Stranex T., Teyssier R., 2013, MNRAS, 436, 2188

Rundle D., Harries T. J., Acreman D. M., Bate M. R., 2010, MNRAS, 407, 986

Sedov L. I., 1959, Similarity and Dimensional Methods in Mechanics. Academic Press, New York

Sod G. A., 1978, J. Comput. Phys., 27, 1

Spitzer L., 1978, Physical Processes in the Interstellar Medium. Wiley-Interscience, New York, p. 333

Stamatellos D., Whitworth A. P., Hubber D. A., 2012, MNRAS, 427, 1182

Strömgren B., 1939, ApJ, 89, 526

Taylor G., 1950, Proc. R. Soc. A, 201, 159

Teyssier R., 2002, A&A, 385, 337

Toro E. F., Spruce M., Speares W., 1994, Shock Waves, 4, 25

Tremblin P., Audit E., Minier V., Schneider N., 2011, in Pogorelov N. V., ed., ASP Conf. Ser. Vol. 444, 5th International Conference of Numerical Modeling of Space Plasma Flows (ASTRONUM 2010). Astron. Soc. Pac., San Francisco, p. 87

Tremblin P., Audit E., Minier V., Schneider N., 2012a, A&A, 538, AA31

Tremblin P., Audit E., Minier V., Schmidt W., Schneider N., 2012b, A&A, 546, AA33

Walch S., Whitworth A., Bisbas T., Hubber D. A., Wuensch R., 2015, MNRAS, 452, 2794

Walch S. K., Whitworth A. P., Bisbas T., Wünsch R., Hubber D., 2012, MNRAS, 427, 625

Walch S., Whitworth A. P., Bisbas T. G., Wünsch R., Hubber D. A., 2013, MNRAS, 435, 917

Walch S. K. et al., 2014, preprint (arXiv:1412.2749)

Whitworth A. P., Bhattal A. S., Chapman S. J., Disney M. J., Turner J. A., 1994a, MNRAS, 268, 291

Whitworth A. P., Bhattal A. S., Chapman S. J., Disney M. J., Turner J. A., 1994b, A&A, 290, 421

Williams R. J. R., 2000, MNRAS, 316, 803

Williams R. J. R., 2002, MNRAS, 331, 693

Wise J. H., Abel T., 2011, MNRAS, 414, 3458

Yorke H. W., 1986, ARA&A, 24, 49

Yorke H. W., Welz A., 1996, A&A, 315, 555

## APPENDIX A: FURTHER PLOTS

Fig. A1 shows density plots of the 3D codes for the 'early phase' test (Test 1-3D; left-hand panel) and the 'late phase' test (Test 2-3D; right-hand panel). Both panels are similar to the plots of Figs 2 and 4. The bars correspond to $1\sigma$ standard deviation from all cells/SPH particles.

Figs A2–A5 show cross-section (slice) plots of all 3D codes for the 'early' and 'late' phase tests at $z = 0$ pc. All 3D grid codes have used the same spatial resolution (128 cells) and mesh geometry (uniform). For the particular case of the SPH code SEREN, we have remapped the SPH particles on the $z = 0$ pc slice and have assumed a $128^2$ resolution (see Price 2007, for further details).
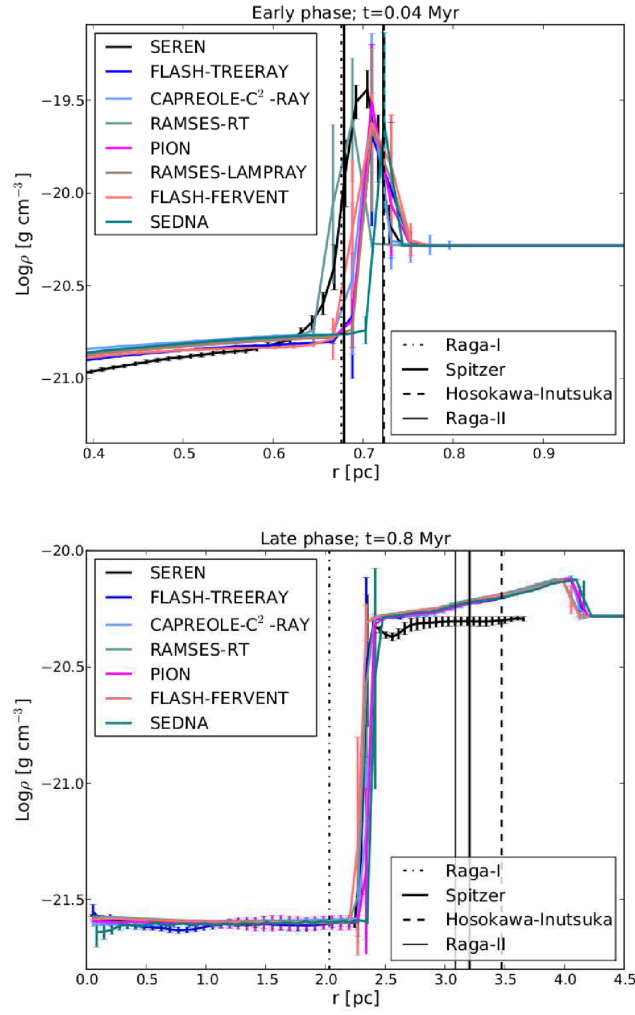
**Figure A1.** Density plots of the early-phase test (Test 1-3D; left) and the late phase test (Test 2-3D; right) for all 3D participating codes. The *x*-axis is in pc and the *y*-axis in $\rho\,\mathrm{cm}^{-3}$. The bars indicate $1\sigma$.
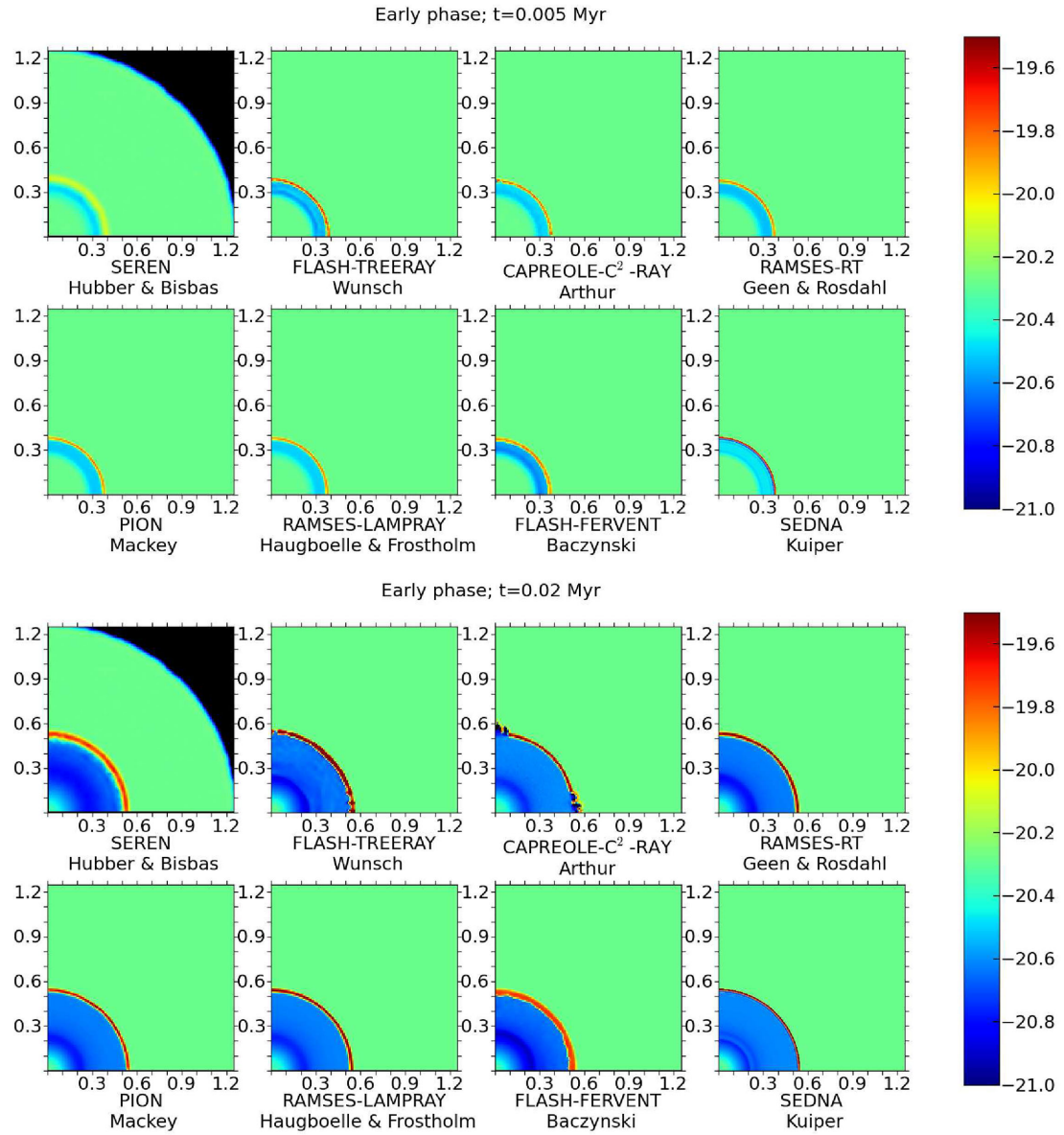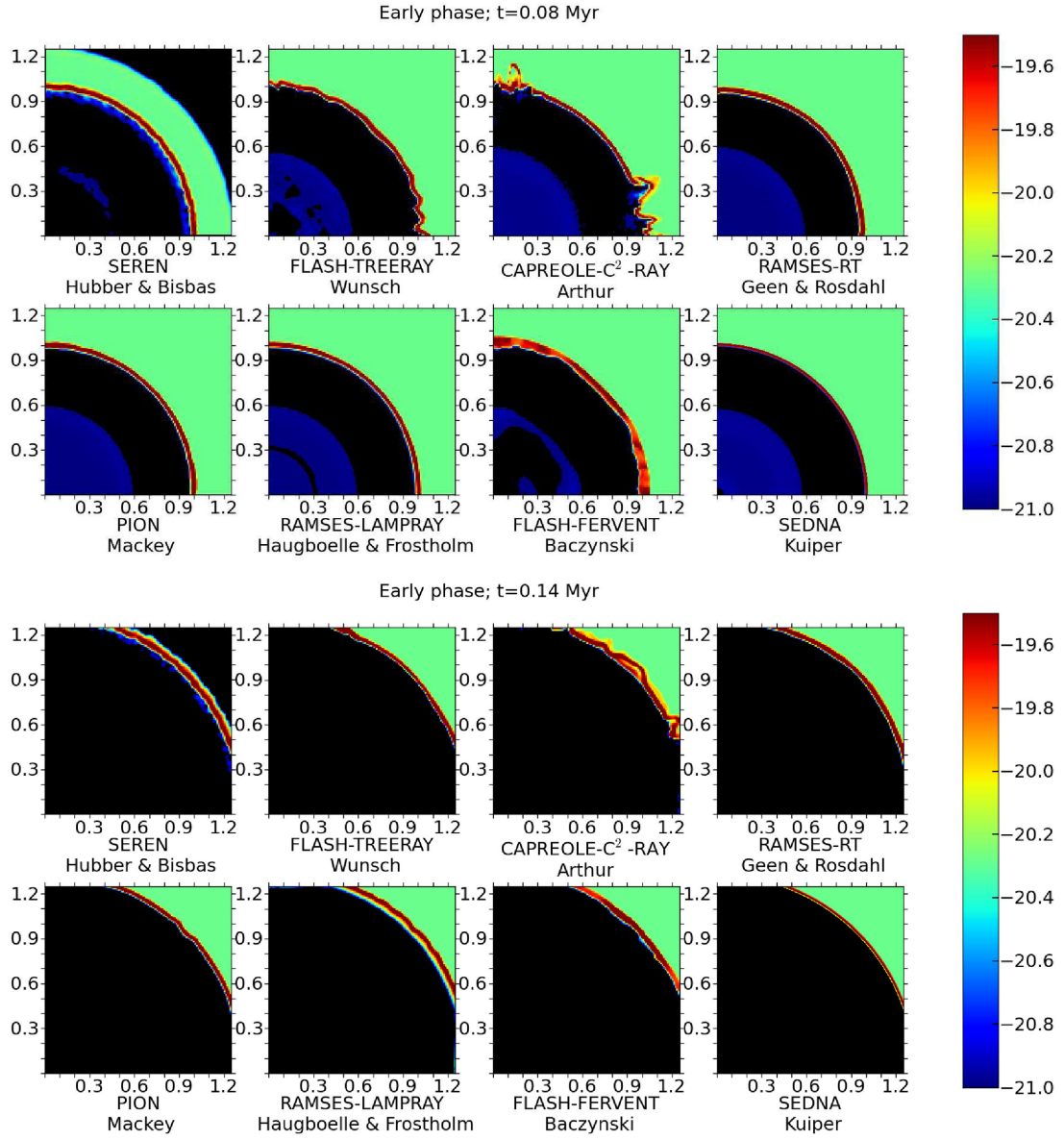
**Figure A2.** Cross-section (slice) plots taken at $z = 0$ pc for the early-phase (Test 1-3D) expansion of all participating 3D codes described in Section 3. $x$- and $y$-axes are in pc. The logarithmic colour bar shows gas density in $\mathrm{g\,cm^{-3}}$. We show snapshots at $t = 0.005$ and $0.02$ Myr.

Early phase; t=0.08 Myr



Early phase; t=0.14 Myr



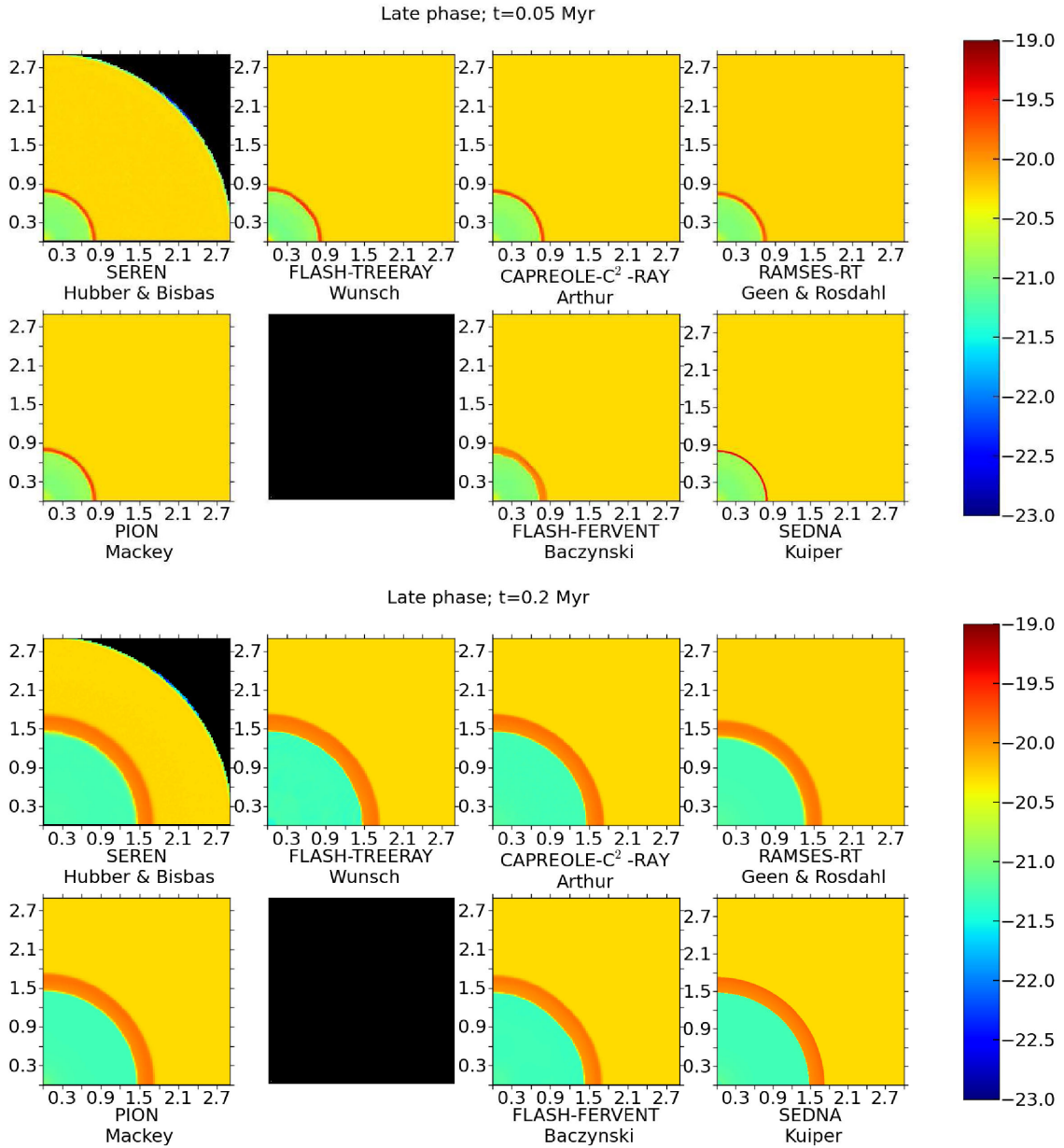**Figure A3.** As in Fig. A2 for $t = 0.08$ and $0.14$ Myr.

**Figure A4.** Cross-section (slice) plots taken at $z = 0$ pc for the late phase (Test 2-3D) expansion of all participating 3D codes described in Section 3. $x$- and $y$-axes are in pc. The logarithmic colour bar shows gas density in g cm$^{-3}$. We show snapshots at $t = 0.05$ and 0.2 Myr.
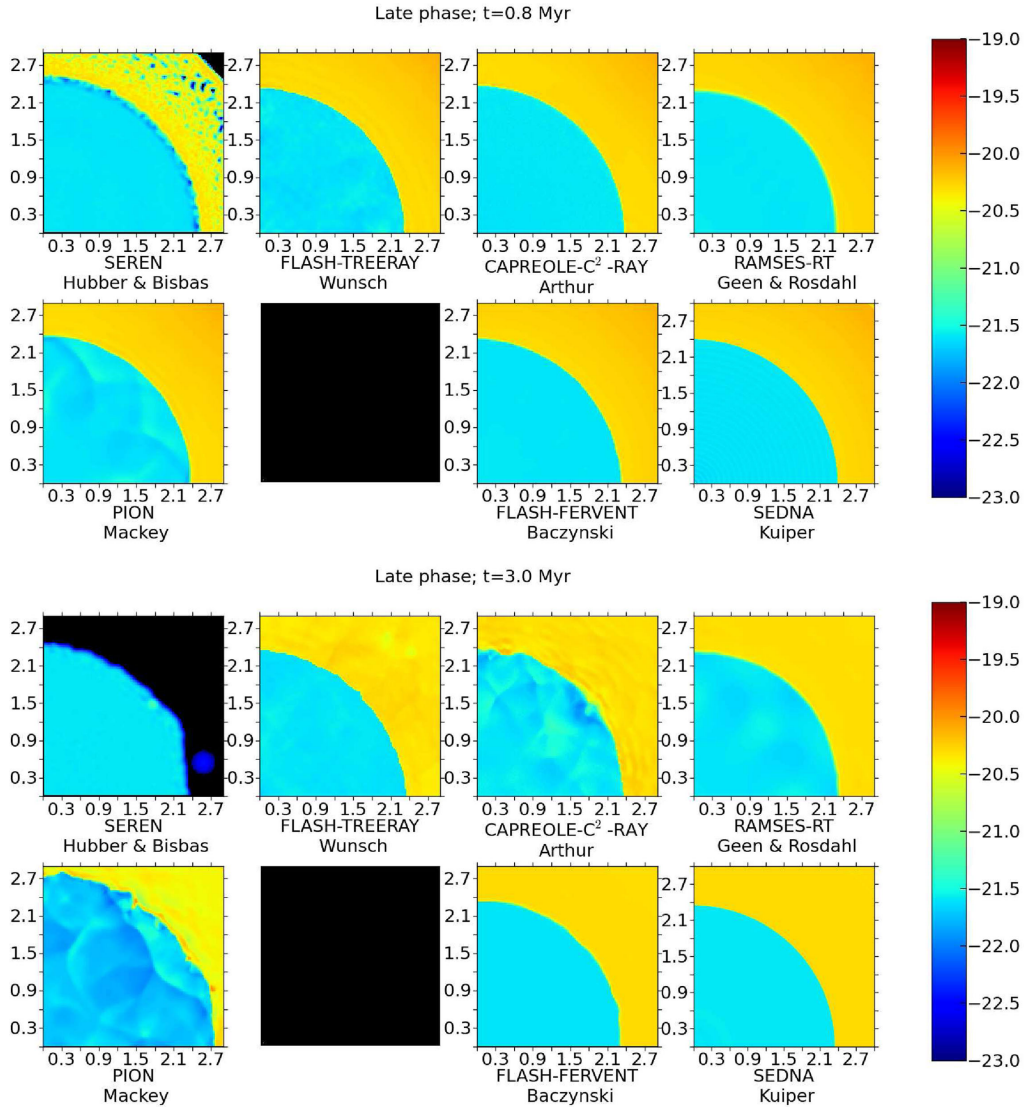
Late phase; t=0.8 Myr



Late phase; t=3.0 Myr



**Figure A5.** As in Fig. A4 but for $t = 0.8$ and $3.0$ Myr.

[1] *University College London, Gower Place, London WC1E 6BT, UK*

[2] *Max-Planck-Institut für Extraterrestrische Physik, Giessenbachstrasse 1, D-85748 Garching, Germany*

[3] *Department of Astronomy and Physics, University of Florida, Gainesville, FL 32611, USA*

[4] *Institute of Astronomy, University of Cambridge, Madingley Road, Cambridge CB3 0HA, UK*

[5] *AWE Aldermaston, Reading RG7 4PR, UK*

[6] *Argelander-Institut für Astronomie, Auf dem Hügel 71, D-53121 Bonn, Germany*

[7] *I. Physikalisches Institut, Universität zu Köln, Zülpicher Strasse 77, D-50937 Köln, Germany*

[8] *Astrophysics Group, University of Exeter, EX4 4, QL Exeter, UK*

[9] *Maison de la Simulation, CEA-CNRS-INRIA-UPS-UVSQ, USR 3441, CEA F-91191 Saclay, France*

[10] *Instituto de Ciencias Nucleares, Universidad Nacional Autónoma de México, Apdo. Postal 70-543, CP: 04510, D.F., Mexico*

[11] *Centro de Radioastronomía y Astrofísica, Universidad Nacional Autónoma de México, Campus Morelia, Apartado Postal 3-72, 58090 Morelia, Michoacán, México*

[12] *Zentrum für Astronomie der Universität Heidelberg, Institut für Theoretische Astrophysik, Albert-Ueberle-Str. 2, D-69120 Heidelberg, Germany*

[13] *University Observatory, Ludwig-Maximilians-University Munich, Scheinerstr.1, D-81679 Munich, Germany*

[14] *Excellence Cluster Universe, Boltzmannstr. 2, D-85748 Garching, Germany*

[15] *Centre for Star and Planet Formation, Natural History Museum of Denmark and Niels Bohr Institute, University of Copenhagen, Øster Voldgade 5-7, DK-1350 Copenhagen, Denmark*

[16] *Laboratoire AIM, Paris-Saclay, CEA/IRFU/SAp - CNRS - Université Paris Diderot, F-91191 Gif-sur-Yvette Cedex, France*

[17] *Department of Physics and Astronomy, University of Sussex, Falmer, Brighton BN1 9QH, UK*

[18] *Institute of Astronomy and Astrophysics, Auf der Morgenstelle 10, D-72076 Tübingen, Germany*

[19] *Max-Planck-Institut für Astronomie, Königstuhl 17, D-69117 Heidelberg, Germany*

[20] *Leiden Observatory, Leiden University, PO Box 9513, NL-2300 RA Leiden, the Netherlands*

[21] *Astronomical Institute, The Czech Academy of Sciences, BočníII 1401, CZ-14131 Prague, Czech Republic*

This paper has been typeset from a TEX/LATEX file prepared by the author.